

Perspective

Combining machine learning with 3D-CFD modeling for optimizing a DISI engine performance during cold-start



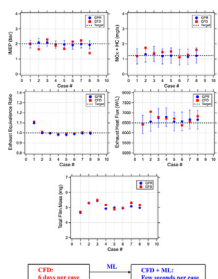
Arun C. Ravindran*, Sage L. Kokjohn

Department of Mechanical Engineering, University of Wisconsin-Madison, Madison, WI 53706, USA

HIGHLIGHTS

- Machine learning for 3D CFD modeling in engine research.
- Machine learning for optimizing engine performance.
- Machine learning for optimizing cold-start performance of DISI engines.
- Machine learning assisted CFD modeling with acceptable accuracy and a substantial reduction in the computational cost.
- The most promising modeling strategy for engine industry : machine learning combined with RANS.

GRAPHICAL ABSTRACT



ARTICLE INFO

Article history:

Received 15 January 2021

Received in revised form 26 March 2021

Accepted 30 March 2021

Available online 6 April 2021

ABSTRACT

This work presents a methodology for using machine learning (ML) techniques in combination with 3D computational fluid dynamics (CFD) modeling to optimize the cold-start fast-idle phase of a gasoline direct injection spark ignition (DISI) engine. The optimization process implies the identification of the range of operating parameters, that will ensure the following criteria under cold-start conditions: (1) a fixed IMEP of 2 bar (BMEP of 0 bar), (2) a stoichiometric exhaust equivalence ratio (based on carbon-to-oxygen atoms) to ensure the efficient operation of the after-treatment system, (3) enough exhaust heat flux to ensure a rapid light-off of the after-treatment system, and (4) reduced NOx and HC emissions. A total of six operating parameters will be identified as having a significant influence on cold-start engine performance. These parameters are associated with the fuel injection strategy (end of the second injection, injection pressure, and fuel mass); combustion strategy (spark timing, spark energy); and intake airflow (intake manifold pressure). Performing an optimization study exclusively using multi-cycle (at least 3 cycles) 3D CFD simulations would be an arduous task. For example, to achieve an exhaust equivalence ratio of 1 and an IMEP of 2 bar, multiple iterations would be required for fuel mass (to account for film formation), intake manifold pressure (to ensure enough air in-cylinder), and spark timing (to ensure the fixed load). This process would be more convoluted and expensive with the addition of constraints for exhaust heat flux and emissions. A promising approach to tackling such a complicated optimization process is to employ the concept of machine learning, which demands a database formed by the six operating parameters mentioned above. The current work will demonstrate a strategy of combining CFD modeling with advanced Gaussian Process Regression (GPR)-based ML models to make predictions about DISI cold-start behavior with acceptable accuracy and a substantially reduced computational time.

Introduction

The light-duty vehicle (LDV) market has received aggressive regulatory policies to secure an overall reduction in fuel use and greenhouse

gas (GHG) emissions. For example, in the United States (US), the Environmental Protection Agency (EPA) and the National Highway Traffic Safety Administration (NHTSA) have adopted standards for the LDV market that will reduce the carbon dioxide (CO_2) emissions from new vehicles by around 50% by 2025, an annual reduction estimated of approximately 4.8% [1]. These organizations have estimated that such an accomplishment for the LDV market is possible via technologies such as

* Corresponding author.

E-mail address: aravindran3@wisc.edu (A.C. Ravindran).

Table 1
Constraints mandated for cold-start operating conditions.

Constraints	Values
NOx + HC	< 1.25 mg/s
Exhaust heat flux	> 6500 W/L
Exhaust equivalence ratio	0.98 – 1.02
Intake mean effective pressure (IMEP)	1.9 – 2.1 bar

downsized turbocharged gasoline direct-injection engines with cooled exhaust gas recirculation [2]. The result is a steep increase in the market penetration of gasoline direct-injection engines in the LDV market - 50% in the United States by 2016 [3]. Despite the advantages of CO₂ reduction demonstrated by these engines, the direct-injection strategies adopted have resulted in serious emission challenges, particularly during the cold-start phase of its operation.

In the EPA Urban Dynamometer Driving Schedule (UDDS), which represents the city driving conditions for LDVs, the cold-start phase is defined as the first 505 s of the test drive cycle. It has been reported that approximately 79% of HC emissions and 58% of NOx emissions for the entire EPA FTP75 drive cycle are formed during this cold-start phase [4]. Within this cold-start phase, the early engine crank-start, followed by approximately 20 s of cold-start, fast-idle phases are responsible for the major share of emissions [5,6]. The emission control in gasoline engines is usually achieved by installing three-way catalysts (TWCs) in the exhaust system, which is extremely effective in simultaneously removing three of the pollutants—CO, HC, and NOx [7]. The TWCs offer high conversion efficiencies for all three of these pollutants when two conditions are met: (1) the operating temperature is above its light-off temperature, which is typically around 200 °C, and (2) the air/fuel ratios at the exhaust are near the stoichiometric value. If these conditions are not met, these catalysts are relatively ineffective. As a result, its performance is immensely challenged during the cold-start phase, particularly because of its relatively lower operating temperatures.

The cold-start phase presented in this work represents the duration between 5 s (after the engine speed flare) to 20 s of the EPA FTP-75 drive cycle, where the engine runs at the targeted cold-start fast-idle speed (1250 rpm for the engine studied in this work as shown in Table 3). Multiple challenges need to be addressed for optimizing the engine performance for the cold-start phase: (1) maintaining a stoichiometric equivalence ratio (based on carbon-to-oxygen atoms) at the exhaust for the efficient operation of the after-treatment system, (2) reducing the NOx and HC emissions, (3) ensuring enough exhaust heat flux for a rapid light-off of the after-treatment system, all while maintaining a fixed load of 2 bar IMEP (BMEP of 0 bar). Addressing all of these challenges would demand a deeper insight into the various phenomenon happening in-cylinder for which an experimental brute-force approach would be an impractical task. The most promising solution for addressing these challenges is multi-dimensional modeling utilizing advanced CFD codes, as evident from the extensive literature on its successful applications. Table 1 quantifies the different constraints to be followed for the current cold-start optimization study as mandated by the industrial partner.

For the current work, a total of six operating/design parameters were identified as having significant influences on the cold-start engine performance. These parameters were identified based on the discussions with the industrial partner. The parameters are associated with the fuel injection strategy (end of the second injection, injection pressure, and fuel mass); combustion strategy (spark timing, spark energy); and intake airflow (intake manifold pressure). Performing an optimization study exclusively using multi-cycle (at least 3 cycles) 3D CFD simulations would be taxing. Simulating three cycles for the single-cylinder version of a 2.3 L spray-guided (SG) DISI engine under cold-start conditions and using two nodes (16 cores per node, 8 GB per core) took approximately six days in the high-performance computational (HPC) facility at the University of Wisconsin–Madison. Unlike normal operating conditions,

there is a substantial amount of wall film formation under the cold-start. The wall-film mass, represented as Lagrangian parcels, is accumulated and carried over from the previous cycles to the next one. As a result, the simulation time for the cold-start substantially increased with the number of cycles because of the time spent solving the conservation equations of the accumulated wall-film parcels.

A large number of these simulations to be run to identify the operating conditions that would meet all of the constraints raises concerns of whether CFD alone would be the right tool for performing this optimization study. For example, to achieve an exhaust equivalence ratio of 1 and an IMEP of 2 bar, multiple iterations would be required for fuel mass (to account for film formation), intake manifold pressure (to ensure enough air within the cylinder), and spark timing (to ensure the fixed load). This process would be more convoluted and expensive with the addition of constraints for exhaust heat flux and emissions. GT-Power might seem to be a potential tool under these circumstances because of its capability to perform multi-cycle simulations of spark-ignited engines [8,9]. However, the applicability of such 1D tools for studying the cold-start phase is questionable because of their inability to handle two important parameters that substantially influence the combustion behavior of the next cycle: (1) in-cylinder stratification produced by the direct injection strategies and (2) wall-film interactions.

A promising approach to tackling such a complicated optimization process is to assist CFD by employing the concepts of machine learning (ML). ML techniques have been effectively used to learn the intricate relationships between variables that play a significant role in the field of engine design [10–19]. For example, Kodavasal et al. [10] used the random forest ML model to study the influence of flame topology and pre-ignition velocity fields on the peak cylinder pressure fluctuations associated with cyclic variations. Moiz et al. [11] used a machine learning-genetic algorithm (ML-GA) approach to optimize the performance and emissions of a heavy-duty GCI engine operating at medium load conditions with a low-octane gasoline-like fuel. Another ML model that has shown high potential with non-parametric data is the kernel-based Gaussian process regression (GPR) model. Kavuri and Kokjohn [12] demonstrated the potential of GPR ML models coupled with CFD-based genetic algorithm optimization to reduce the computational time of the optimization process by 62%. Stepping out of the engine research field, Bin and Wenhai [20] used GPR models to predict thermal comfort index as a function of parameters of activity level, clothing insulation, air temperature, air relative humidity, air velocity, and mean radiant temperature. In comparing the GPR model's performance with other ML models, such as neural networks and support vector machines, these researchers found the GPR model to have relatively higher fitting precision.

Additionally, the GPR approach has been successfully employed in highly diverse areas, such as remote sensing [21,22], music [23], biomedical applications, and health care [24,25]. This convincing background enabled the selection of the GPR model for the current cold-start optimization study. The challenge, however, was designing regression models that could predict the value of a response variable, given a non-parametric training set of a relatively smaller size, with an acceptable accuracy and response time. The current work will demonstrate a strategy of combining CFD modeling with GPR-based machine learning models to make predictions about DISI cold-start behavior with acceptable accuracy and substantially reduced computational times.

Numerical setup

Engine setup

The engine modeled in this work is the single-cylinder version of a 2.3 L spray-guided (SG) injection DISI engine. Table 2 gives an overview of the engine and injector specifications. Details of the cold-start operating conditions modeled for this study are provided in Table 3. After/before top dead center (ATDC/ BTDC) references have been made

Table 2
Engine and Injector specifications of the DISI engines considered for this study.

Engine specifications	SG-DISI engine
Displacement	2.3 L
Bore x Stroke	8.75 cm x 9.4 cm
Compression Ratio (-)	11.46
Injector Specifications	
Number of Holes	6
Hole Diameter	181 μm
Injection Pressure	100 bar
Injection Strategy	Spray Guided Injector

Table 3
Cold-start test conditions for an SG-DISI 2.3 L engine.

SG-DISI 2.3 L Engine	Test 1	Test 2	Test 3
NMEP	2 bar	2 bar	2 bar
Speed	1250 rpm	1250 rpm	1250 rpm
SOI1	300 deg BTDCc	300 deg BTDCc	300 deg BTDCc
SOI2	44 deg BTDCc	44 deg BTDCc	44 deg BTDCc
Split Ratio	75–25%	75–25%	75–25%
Spark timing	26 deg ATDCc	22 deg ATDCc	18 deg ATDCc
EVC	5 deg ATDCi	30 deg ATDCi	55 deg ATDCi
IVO	0 deg ATDCi	0 deg ATDCi	0 deg ATDCi
Intake Duration	240 deg	240 deg	240 deg
Exhaust Duration	210 deg	210 deg	210 deg
EVO	155 deg ATDCc	180 deg ATDCc	205 deg ATDCc
Total fuel mass	27 mg	27 mg	27 mg

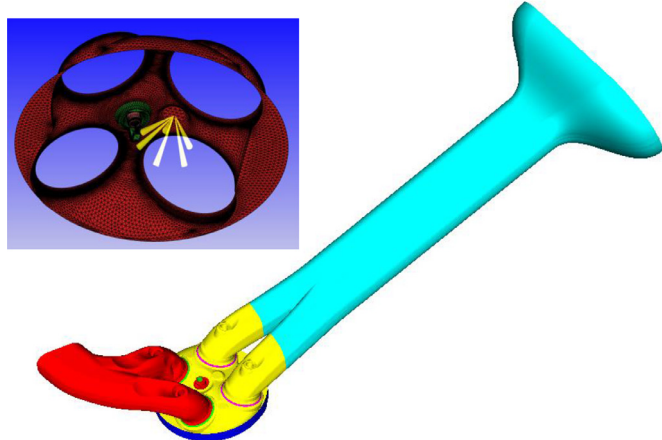


Fig. 1. 2.3 L SG-DISI engine topology.

with respect to combustion or intake stroke TDC, as represented by the subscripts *c* and *i*, respectively. Three conditions were studied, the primary difference between them being the exhaust valve closing (EVC) timing. The engine used a split injection strategy [6], in which 75% of the fuel mass was injected during the intake stroke, and the remaining 25% was injected during the compression stroke. The engine used relatively retarded spark timing under these conditions in an attempt to ensure enough exhaust heat flux for a rapid light-off of the after-treatment system. The retarded spark timing combined with the effects of decaying in-cylinder turbulence can have a substantial effect on cold-start flame behavior, which could be studied in detail by employing a robust turbulence-combustion modeling strategy. The injection strategies used and the topology of the SG-DISI engine are shown in Fig. 1.

Computational model

The 3D CFD simulations presented in this study were performed using the CONVERGE CFD software [26]. Simulating cold-start behavior is challenging because of the wide nature of the phenomenon happen-

ing within the cylinder. An accurate prediction of such conditions involves efficient use of multiple models: spray modeling to capture the split injection strategies, ignition modeling to capture the effects of the retarded spark timing, combustion modeling to accurately capture the flame travel, and turbulence modeling to capture the effect of decaying turbulent kinetic energy. In addition, different physical models are used for capturing wall-film interactions, which is a critical phenomenon observable during cold-start. Different aspects associated with wall films, such as splash, rebound, and wall-film vaporization, were all modeled. However, a detailed discussion of the technical concepts of wall-film modeling is beyond the scope of this paper. Instead, detailed discussions of wall-film modeling under cold-start conditions can be found in a study by Malaguti et al. [27,28].

Table 5 lists the different models used for simulating the cold-start behavior in this study. The flame initiation and subsequent propagation were modeled using the Plasma velocity on G-surface (PVG) ignition model [33] and G-Equation for lower Reynolds number regimes (GLR) combustion model [30], in a RANS framework. Both of these models will be summarized in the upcoming sections. The critical scales of turbulence, which result from the gas exchange processes, were modeled with the renormalization group (RNG) $k-\epsilon$ model. Boundary layer effects on the wall were treated using law-of-the-wall boundary conditions. Thermal boundary conditions for the cold-start phase were based on surface thermocouple measurements that were acquired from an instrumented multi-cylinder engine running at the same operating conditions provided in Table 3. The temperature values for the cold-start were 323 K for the liner, 353 K for the head, and 353 K for the piston.

A base grid size of 4 mm was used for the current cold-start simulations. The spray injection process was initialized with 50,000 Lagrangian spray parcels coupled with the gas phase via source terms in the mass, momentum, and energy equations. The initial phase of the spray breakup was captured using cells of 125 μm in size, achieved through injector embedding. Spray particles outside the embedded region were captured through adaptive mesh refinement (AMR) and cylinder embedding. Constant volume simulations were performed on a vaporizing Spray-G setup from the Engine Combustion Network (ECN) [34], to optimize the KH-RT model constants (Table 4) to capture the correct spray liquid/vapor penetration for the mesh dimensions considered.

The valve motion and film formation required a finer cell layer along the boundary, which was achieved through boundary embedding. A spark plug (a 14 mm plug with 0.7 mm spacing between the electrodes) was included in the engine model to capture the interactions of the fuel spray and spark electrodes. Finally, all variations in the in-cylinder velocity and temperature, resulting from the process of combustion and changing turbulence, were captured utilizing AMR. Although it is impossible to achieve a completely mesh-independent result simultaneously involving all these processes, it was at least ensured that sufficient mesh resolution, as demanded by each model, was available utilizing localized grid control strategies available with CONVERGE.

A multi-component evaporation model was used to capture the vaporization characteristics of gasoline. A 10-component surrogate model was developed via constant volume simulations in CONVERGE, which provided the most accurate representation of the distillation curve and evaporation characteristics of the gasoline. The surrogate models were formulated following the concepts presented by Anand et al. [35]. The species names and compositions used are shown in Table 6.

GLR combustion model

The GLR model is the G-Equation model optimized for an improved performance under cold-start operating conditions. A summarized version of this modification, which is otherwise elaborated in Ravindran et al. [30], will be presented in this section. The turbulent flame speed model from Peters [36] was used to impose the normal propagation velocity of the G-surface. The turbulent flame speed is modeled as follows:

Table 4

Models used for respective in-cylinder phenomenon.

Process	Models	Comments on Model Constants
Spray breakup	KH-RT model [29]	Model constants tuned to match ECN Spray-G measurements: shed_factor = 1.0, kh_cnst1 = 0.188, kh_cnst2 = 7.0
Combustion	GLR [30]	See Section 'GLR combustion model'
Iso-octane laminar flame speed	Gulder model [31]	See Section 'GLR combustion model'
Turbulence	RNG k- ϵ [29]	$C_{\mu} = 0.0845$, $C_{(\epsilon 1)} = 1.42$, $C_{(\epsilon 2)} = 1.68$, $C_{(\epsilon 3)} = -1.0$, $\beta = 0.012$, $\eta_0 = 4.38$, Reciprocal ϵ Prandtl = 1.39, Reciprocal TKE Prandtl = 1.39
Wall film interactions	O'Rourke and Amsden [32]	$E_{crit}^2 = 3330$
Ignition model	PVG ignition model [33]	See Section 'PVG ignition model'
NOx	Extended Zeldovich [7]	See Section 'Emissions modeling'

Table 5

Mesh resolution adopted for modeling respective phenomena.

Phenomenon	Mesh Resolution	Mesh Refinement Strategy (Base Grid = 4 mm)
Spray	250 μ m	Injector embedding Level 4 + AMR Level 3
Ignition	125 μ m	Source embedding Level 5
Temperature and velocity gradients	500 μ m	AMR Level 3
Boundary	500 μ m	Boundary embed Scale 3
Flame travel	500 μ m	Cylinder embedding Level 2 + AMR (velocity and temperature) Level 3

Table 6

Multi-component surrogate model used to capture Gasoline.

Component name	Component	Mass fraction
Iso-pentane	ic5h12	0.125
Pentene	c5h10	0.010
n-Pentane	nc5h12	0.020
Cyclo-pentane	cyc5h10	0.100
Iso-octane	ic8h18	0.335
Toluene	c7h8	0.140
Iso-cumene	ic9h12	0.050
Decane	c10h22	0.080
Tetralin	c10h12	0.090
Butane	c4h10	0.050

$$S_T = S_L + u' \left\{ -\frac{a_4 b_3^2}{2b_1} Da + \left[\left(\frac{a_4 b_3^2}{2b_1} Da \right)^2 + a_4 b_3^2 Da \right]^{1/2} \right\}, \quad (1)$$

where u' is the root mean square of the turbulent fluctuating velocity, S_L is the unstretched laminar flame speed, Da is the Damköhler number. a_4 is a derived quantity, the value of which is 0.78 [37]. The laminar flame speed (S_L) was modeled using the Gulder model [31]. The laminar flame speed of gasoline and iso-octane were closely comparable, as presented by Heywood [7]. Accordingly, gasoline was represented using iso-octane in this study. For this study, b_1 was adjusted to 2, based on the experimental data from Bradley et al. [38]. S_T is the local turbulent flame speed modeled using the theory proposed by Peters [36], modified to include the effects of flame surface wrinkling as the flame traveled through different regimes of the Borghi–Peters regime diagram.

$$b_3 = \min \left[\left(C_0 + C_1 \log \left(\frac{u'}{S_L} \right) + C_2 \log \left(\frac{1}{l_f} \right) + C_3 \left[\log \left(\frac{u'}{S_L} \right) \right]^2 \right) * \max \left\{ 1, \left(\frac{Re_{local}}{56} \right) \right\} \right], 2 \quad (2)$$

The constants are $C_0 = 0.077226$, $C_1 = 1.51206$, $C_2 = 0.95855$, $C_3 = -0.836646$, and $C_4 = -0.521226$.

The value of b_3 was determined by the expression in the inner curly brackets until the turbulent Reynolds number value of 56. Beyond this value, the result from the expression was multiplied by the ratio of the local Reynolds number to 56, following a constant Karlovitz line, until

b_3 obtained a value of 2. A detailed explanation of the calculation, including the significance of each number presented here, can be found in Ravindran et al. [30].

PVG ignition model

The plasma velocity on G-surface (PVG) is a phenomenological ignition model to capture the early flame growth resulting from the spark ignition process in a DISI engine and thus responds to the effects of changing spark energy. A summarized description of this model, which is otherwise elaborated upon in Ravindran [33], will be presented in this section. The PVG model accounts for the effects of plasma expansion and local mixture properties such as turbulence and the equivalence ratio on the early flame growth. Beyond this, the sub-model for capturing the plasma expansion velocity (S_{Plasma}) was derived based on the theory used by the DPIK model [39],

$$S_{Plasma} = \frac{\dot{Q}_{spark} \eta_{eff}}{4\pi r_k^2 \left[\rho_u (u_k - h_u) + P \frac{\rho_u}{\rho_k} \right]} \quad (3)$$

where \dot{Q}_{spark} is the spark energy discharge rate during the breakdown phase, which according to Heywood [7] could be as high as 1 MW, although the total spark energy could be as small as 0.3 to 1 mJ. In addition, η_{eff} is the efficiency at which the supplied spark energy is transmitted to the gas mixture and is governed by the heat loss to the electrodes during each discharge mode of the spark discharge process [7]. A value of 0.3 for η_{eff} was used in this study. Next, h_u is the specific enthalpy of the unburned mixture, and u_k is the specific internal energy of the burned mixture inside the G-surface. Finally, ρ_u is the local unburnt gas density, P is the pressure, and r_k is the instantaneous flame kernel radius.

The local turbulent flame speed was captured using the Peters model, the accuracy of which was improved by dynamically modeling the constant b_3 . The concept used for modeling b_3 was derived from the GLR model [30], as shown in Eq. (2). The plasma velocity and local turbulent flame speeds thus obtained were applied on a G-surface initialized in the spark region at the spark timing representing the first ignition kernel. The initial flame kernel was marked using a quasi-laminar G-surface of, for example, a 0.5 mm radius, which was resolved using the local mesh-embedding techniques available in CONVERGE.

Table 7
GPR model kernel functions that assume the same length scale for each predictor.

Kernel Function	Formulation
Squared Exponential	$k(x_i, x_j) = \sigma_f^2 \exp\left[-\frac{1}{2} \frac{r^2}{\sigma_f^2}\right]$
Exponential	$k(x_i, x_j) = \sigma_f^2 \exp\left(-\frac{r}{\sigma_f}\right)$
Matern 3/2	$k(x_i, x_j) = \sigma_f^2 \left(1 + \frac{\sqrt{3}r}{\sigma_f}\right) \exp\left[-\frac{\sqrt{3}r}{\sigma_f}\right]$
Matern 5/2	$k(x_i, x_j) = \sigma_f^2 \left(1 + \frac{\sqrt{5}r}{\sigma_f} + \frac{5r^2}{3\sigma_f^2}\right) \exp\left[-\frac{\sqrt{5}r}{\sigma_f}\right]$
Rational Quadratic	$k(x_i, x_j) = \sigma_f^2 \left(1 + \frac{r^2}{2\alpha\sigma_f^2}\right)^{-\alpha}$, where α is a positive valued scale-mixture parameter where $r = \sqrt{(x_i - x_j)^T (x_i - x_j)}$

Table 8
GPR model kernel functions that assume separate length scale for each predictor.

Kernel Function	Formulation
ARD Squared Exponential	$k(x_i, x_j) = \sigma_f^2 \exp\left[-r^2\right]$
ARD Exponential	$k(x_i, x_j) = \sigma_f^2 \exp\left(-r\right)$
ARD Matern 3/2	$k(x_i, x_j) = \sigma_f^2 \left(1 + \sqrt{3}r\right) \exp\left[-\sqrt{3}r\right]$
ARD Matern 5/2	$k(x_i, x_j) = \sigma_f^2 \left(1 + \sqrt{5}r + 5r^2\right) \exp\left[-\sqrt{5}r\right]$
ARD Rational Quadratic	$k(x_i, x_j) = \sigma_f^2 \left(1 + \frac{r^2}{2\alpha}\right)^{-\alpha}$, where α is a positively valued scale-mixture parameter where $r = \sqrt{\sum_{m=1}^d \frac{(x_{im} - x_{jm})^2}{\sigma_m^2}}$ $m = 1, 2, \dots, d$ σ_m is the individual length scale for each predictor m

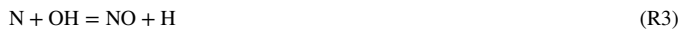
Table 9

Parameters considered for developing the non-parametric CFD database, which serves as the training set for the GPR models.

Parameter	Description	Units	Baseline	Min	Max
EOI2	End of the second injection	deg BTDCc	35	20	90
IP	Injection pressure	bar	140	140	500
ST	Spark timing	deg ATDCc	24.2	14	40
SE	Spark energy	W	n/a	10	100
FM	Fuel mass	mg	27	23.76	30.24
IMAP	Intake manifold pressure	Pa	74,594	67,094	82,094

Emissions modeling

In this section, the modeling strategy employed for NOx and HC emissions will be explained. There are three major components in the exhaust gases of a spark-ignited engine: nitric oxide, NO, and small amounts of nitrogen dioxide, collectively known as NOx, carbon monoxide (CO), and organic compounds left behind as partially burned or unburned hydrocarbons (HC). NOx and HC were the primary interest of the current study. NOx emissions were modeled using the extended Zeldovich mechanism, which considers the following to be the principal reactions governing the formation (and destruction) of NO from molecular nitrogen:



The forward and reverse rate constants for these reactions have been measured in numerous experimental studies, a summarized version of which was presented in Heywood [7]. Each of the rate constants for these reactions has an associated uncertainty factor, also provided in Heywood [7]. For the current work, the NOx predictions in comparison to the measured values were improved by applying a correction factor of 1.2 for the forward rate constant of R1, 0.2 for the reverse rate constant of R2, and 0.3 for the reverse rate constant of R3. Next, the NO so predicted was converted to NOx by applying a factor of 1.533, which is the ratio of the molecular weight of NO₂ to NO. The rate constant

correction factors had to be applied to account for the complex relationships between the factors responsible for the NOx formation under the cold-start conditions. Three factors governed the NOx formation: (1) in-cylinder fuel/air equivalence ratio, (2) spark timing, and (3) internal residual fraction. The increased level of stratification resulting from the direct injection strategies resulted in a varying local equivalence ratio. The delayed spark timing (>20 deg ATDCc for this study) employed for achieving higher exhaust heat flux led to a higher temperature at the exhaust valve opening (EVO) and a decrease in the internal residual fraction due to the lower density of the exhaust gases. Hence, unlike the normal operating conditions, during the cold-start phase, a delay in the spark timing displayed an increasing trend for NOx (see Fig. 5).

Five potential reasons have been identified for HC emission formation under the cold-start conditions:

- 1 The reduced efficiency of combustion associated with the delayed spark timing acts as a key source for the formation of the HC emissions.
- 2 The reduction in the in-cylinder peak pressure due to the delayed spark timing leads to reduced in-crevice storage of the unburned mixture.
- 3 The delayed spark timing results in a relatively higher post-flame and exhaust temperature, that helps with oxidizing the HC emissions.
- 4 The vaporizing wall film under post-flame conditions contributes to the HC emissions; and
- 5 The cold-start conditions employ a delayed exhaust valve opening (EVO), such as 180 deg ATDCc combined with a valve overlap of 30 deg (Test #2) as shown in Table 3. This strategy was adopted to

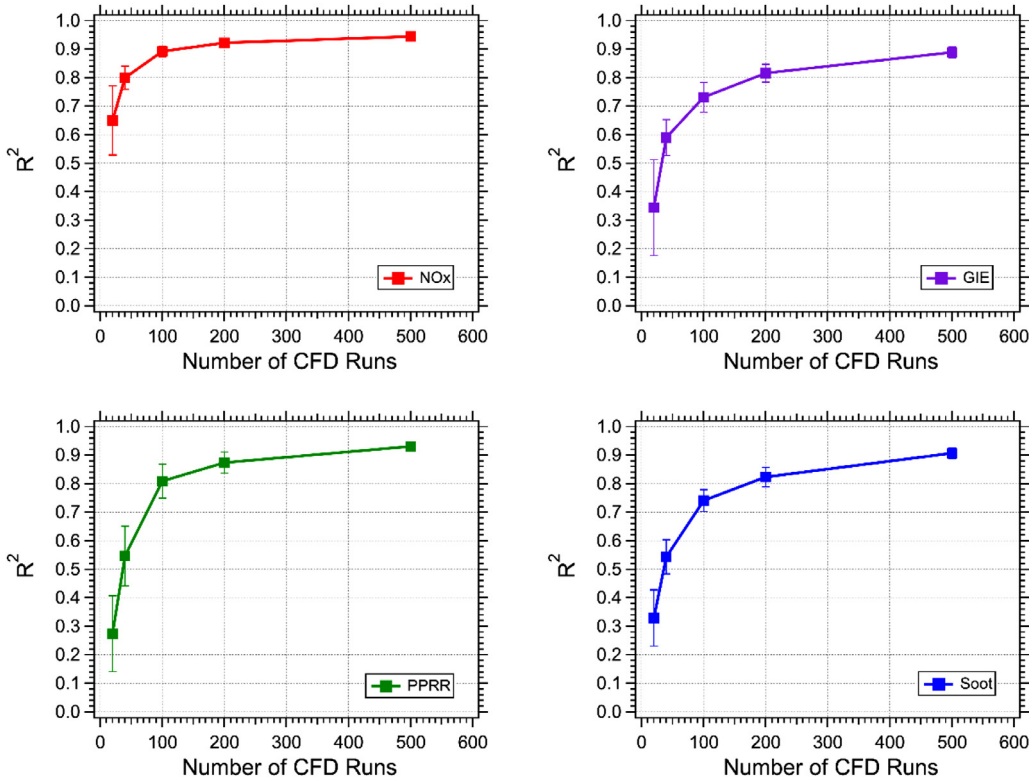


Fig. 2. R^2 dependence on the dataset size studied using the data provided by Kavuri and Kokjohn [12].

Table 10

Response variables considered for the study.

Response variables	Description	Units	Comments
1 NOx	NOx emissions	mg/s	Flow rate at the exhaust runner outlet
2 HC	Unburned hydrocarbon emissions	mg/s	Flow rate at the exhaust runner outlet
3 Phi_Exhaust	Exhaust equivalence ratio	-	Mean value between EVO and EVC
4 IMEP	Indicated Mean Effective Pressure	bar	
5 CA50	50% of total heat release	deg ATDCc	
6 EHF	Exhaust heat flux	W/L	Exhaust energy from EVO to end of the cycle
7 Total Film Mass	Sum of film mass on liner, piston, and head	mg	Total film mass at the end of the cycle
8 TEVO	Temperature at the exhaust valve opening	K	Temperature at EVO
9 CHRR	Cumulative apparent heat release rate (AHRR)	J	Cumulative AHRR at EVO

facilitate the re-breathing of the exhaust, thereby enhancing the HC oxidation.

The multi-cycle simulations performed in this study by employing the models and mesh strategies explained earlier helped to capture all of these factors leading to the formation of the NOx and HC emissions. Detailed validations of the CFD models to the experimental data for the three cold-start fast-idle conditions provided in Table 3 are included in the appendix.

ML regression approach

GPR models

This section will briefly describe the theory governing the Gaussian process regression (GPR) models. GPR is a nonparametric probabilistic model that works on the Bayesian approach. A simplified regression model is given as follows:

$$y = f(x) + \epsilon \quad (4)$$

where y is the dependent variable, x is the independent vector, $f(x)$ is the regression function to be estimated, and ϵ is the noise between the

dependent variable and the regression function. In the GPR modeling approach, this regression function, $f(x)$, is assumed to follow a Gaussian process (GP), which means the function $f(x)$ is related to the independent vector x via a Gaussian distribution:

$$f(x) = GP[\mu(x), k(x, x')] \quad (5)$$

where $\mu(x)$ is the mean function of the input vector x , and $k(x, x')$ is the covariance function over the two inputs x and x' . With the GPR approach, the mean function is assumed to have zero value. The noise is assumed to follow a Gaussian distribution, also with a zero mean and a noise variance σ_n^2 such that $\epsilon \approx N(0, \sigma_n^2)$. With the assumption of both the GP function of the regression function and the mean of the Gaussian noise following a zero mean function, the dependent variable y will also follow a GP with a zero mean function and a covariance function $k_{noise}(x_i, x_j)$, accounting for the effect of noise. In addition, x_i and x_j are two D -by-1 input vectors.

$$y \approx GP[0, k_{noise}(x_i, x_j)] \quad (6)$$

The noisy covariance function is related to the covariance function of the regression function as follows:

$$k_{noise}(x_i, x_j) = k(x_i, x_j) + \sigma_n^2 \delta_{ij} \quad (7)$$

Table 11
Details of the kernel function combinations used for each response variable.

Response	Kernel Function	R^2 /RMSE
NOx	Average from: ARD Exponential, ARD Matern 5/2, ARD Matern 3/2, ARD Squared Exponential	0.80/0.35044 mg/s
HC	Matern 3/2	0.80/0.96724 mg/s
Phi_Exhaust	ARD Matern 3/2	0.99/0.0056
IMEP	Exponential	0.93/0.2616 bar
CA50	ARD Matern 5/2	0.94/4.22 deg
EHF	ARD Squared Exponential	0.79/462.38 W/L
Total film mass	ARD Matern 5/2	0.90/0.0892 mg
Film piston	ARD Matern 5/2	0.99/0.0971 mg
Film liner	ARD Matern 5/2	0.98/0.03916 mg
Film head	ARD Squared Exponential	0.75/0.0151 mg
TEVO	Average from: ARD Exponential, ARD Matern 5/2, ARD Matern 3/2, ARD Squared Exponential	0.72/70.97 K
CHRR	Matern 3/2	0.91/34.619 J

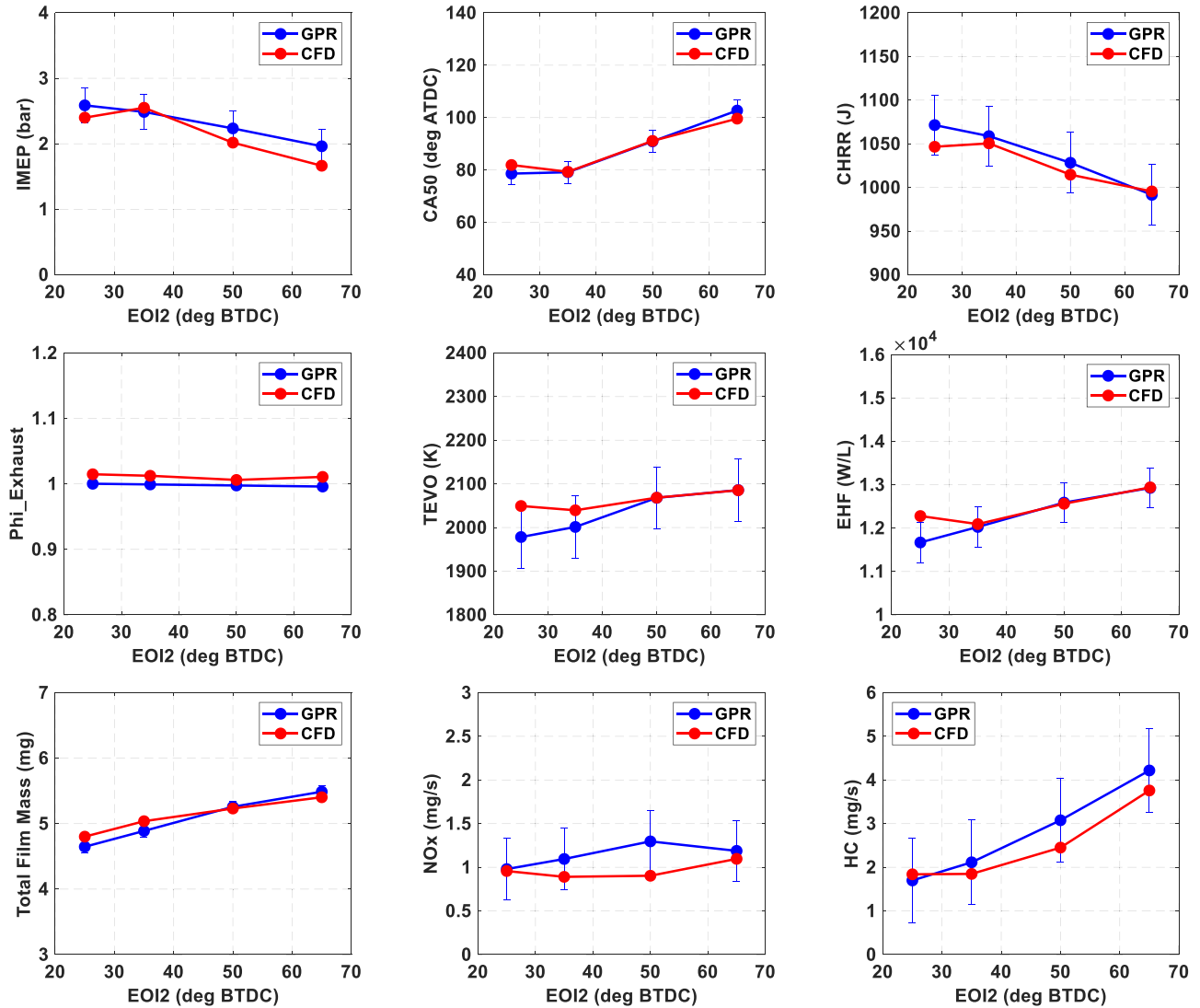


Fig. 3. GPR predictions for EOI2 sweep validated against CFD results.

where δ is the Kronecker delta.

The flexibility of the GPR model arises from the many different kernel functions available to model the covariance function $k(x_i, x_j)$. These kernel functions are based on two parameters: the signal standard deviation σ_f and characteristic length scale σ_l . Table 7 provides the details of the five kernel functions used for this study. The same kernel functions could be used with a separate characteristic length scale σ_m for

each predictor m ($m = 1, 2, \dots, d$), implementing automatic relevance determination (ARD), as listed in

Table 8. The ARD kernel functions were found to perform better with relatively smaller datasets, in which the response variables were found to have varying sensitivity to each variable in the predictor set. This concept was well explored in the current study, as will be explained in the upcoming sections of this paper.

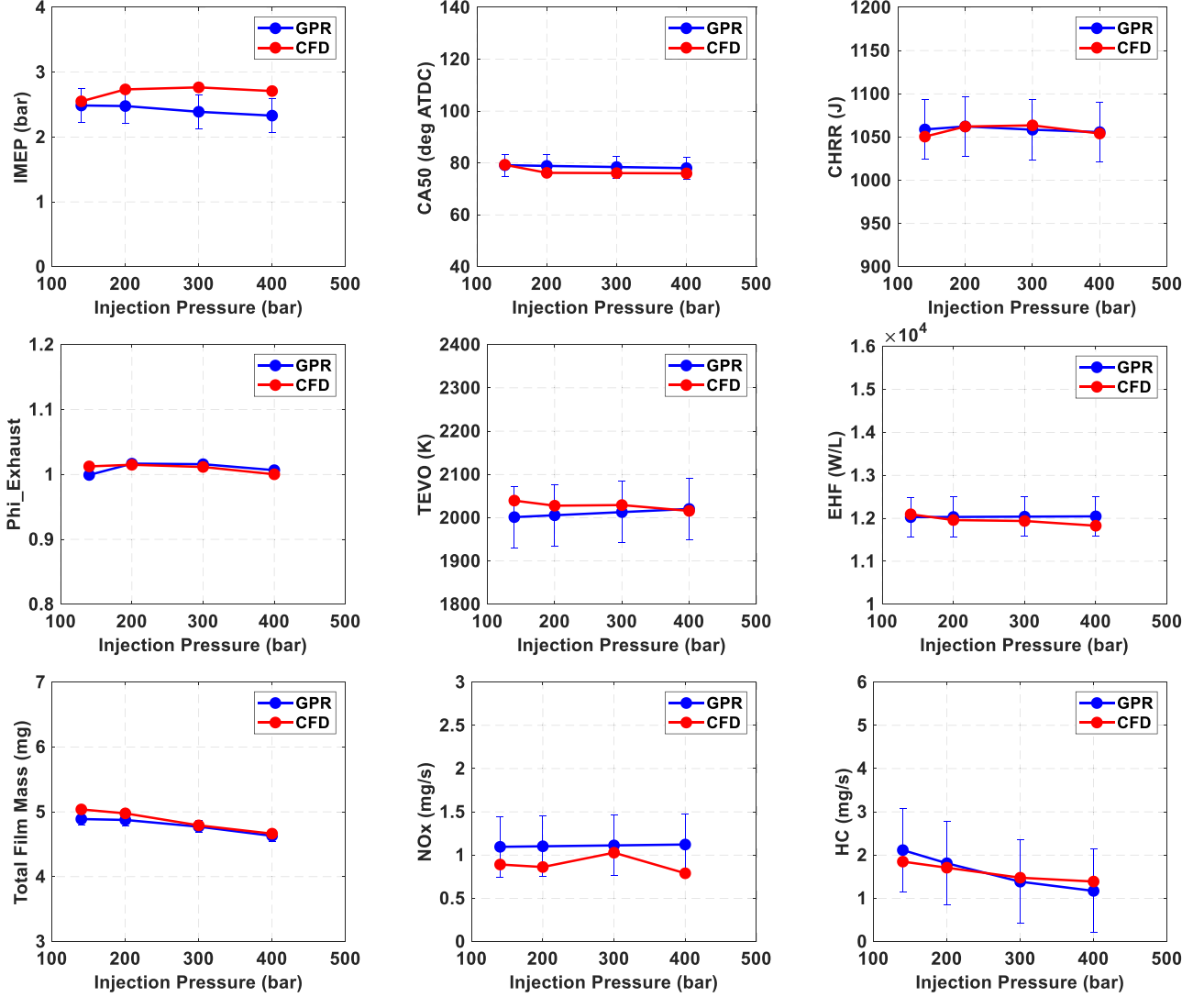


Fig. 4. GPR predictions for injection pressure sweep validated against CFD results.

Table 12
Formulation of the validation set (the number in bold represent the baseline values).

Predictor	Levels
EOI2 (deg BTDC)	25, 35, 50, 65
Injection pressure (bar)	140 , 200, 300, 400
Spark timing (deg ATDC)	14.2, 18.2 , 22.2
Spark energy (W)	10 , 40, 100
Fuel mass (mg)	25, 27 , 29
IMAP (Pa)	80,561, 74,594 , 68,626

Latin hypercube formulation of the training set

Table 9 shows the design parameters that were considered and their respective ranges of variation. Test #2 was used as the baseline for developing the dataset. All other parameters not considered here will essentially use the baseline values of Test #2, as provided in Table 3. It is important to note that each of these design parameters interacts with each other, meaning changing one can affect the others. For example, to achieve an EOI2 of 90 deg BTDC, the start of the second injection (SOI2) needs to be estimated considering the fuel mass and injection pressure of that particular sample.

The statistical method of Latin hypercube sampling was used for generating the random samples distributed over the six input parameters and their respective ranges, as mentioned in Table 9. The number of samples was decided based on an analysis of the engine performance dataset generated by Kavuri and Kokjohn [12]. This dataset was generated using CFD simulations, for optimizing the performance of a high-load, dual-fuel, gasoline-diesel RCCI engine. The input parameters included premix-gasoline-fraction (fraction of total gasoline that is premixed), gasoline-fraction (fraction of total fuel that is gasoline), SOI-gasoline, and SOI-diesel. The output variables were NOx (g/kg-fuel), soot (g/kg-fuel), gross indicated efficiency (GIE) (%), and peak pressure rise rate (PPRR) (bar/deg).

The dataset was used to study the effect of the number of data points on the R^2 value obtained from the different GPR models. The study was performed in MATLAB. Of the total 4500 data points available, 3500 were selected as the training set, and the remaining 1000 composed the validation set. Training sets of different sizes (20, 40, 100, 200, and 500) were sampled from the available 3500 points, and GPR models were fit to the data. Using the input parameters as predictors, separate GPR models were trained for each output (or response) variable. Overfitting was avoided by using the k-fold [40] cross-validation method with a value of 5. In this method, the training set was partitioned into five randomly chosen folds of roughly equal size. One subset was used to

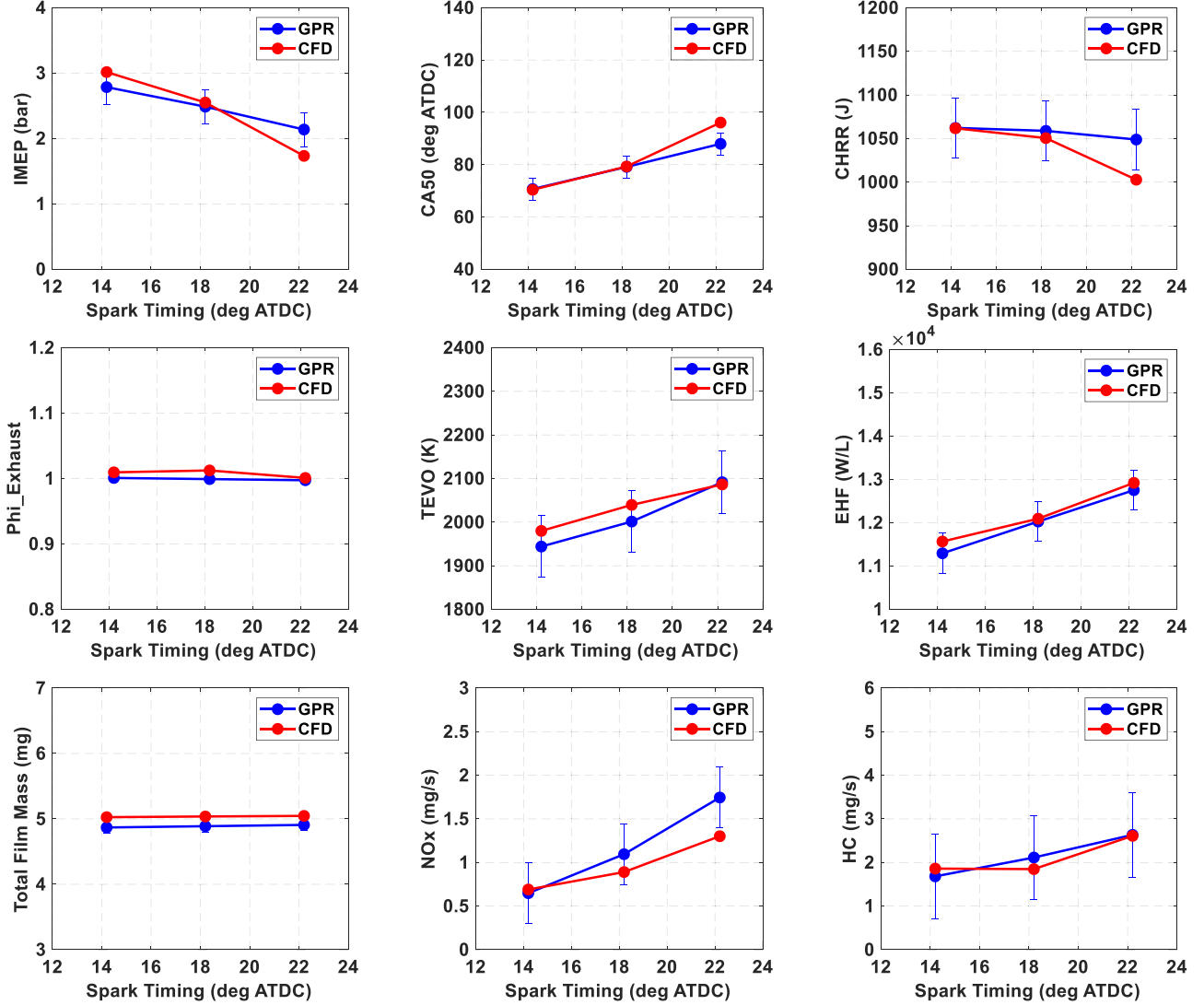


Fig. 5. GPR predictions for spark timing sweep validated against CFD results.

validate the model trained using the remaining subsets. This process was repeated five times so that each subset was used exactly once for validation.

Twenty sets of iterations with varying data were run with each sample size to estimate the mean and the standard deviation of the R^2 value obtained with each model. This practice eliminated any bias of the dataset selected for the training. This procedure was repeated with the GPR models listed in Tables 7-8, and the best performing model giving the highest R^2 value was selected for each sample size. It is important to note that the data from Kavuri and Kokjohn [11] are used only for two purposes: (1) to evaluate the performance of the GPR models (2) identify the sample size requirements for achieving reasonable R^2 values. Hence, the intrinsic details of these datasets, such as engine/injector geometry, CFD models, boundary conditions, etc. are not important to be explained here.

Fig. 2 shows the R^2 value given by the best performing GPR model as a function of the number of data points for all the four output variables. Two trends are predominant with the increasing sample size irrespective of the response variable considered – an increasing trend for R^2 and a decreasing trend for its variation. In addition, 100 data points seemed to be a reasonable estimate to have an R^2 of 0.9 for NOx, 0.73 for GIE, 0.8 for PPRR, and 0.74 for soot. Although the input and output variables for this dataset did not match with the current study, the lessons

learned were used to decide on a starting sample size of 25 data points per predictor variable.

3D CFD simulations were performed on each sample, and a database was built including critical performance-related parameters, shown in Table 10. Three cycles were run for each sample, the first two to remove the uncertainties associated with the initial conditions, to get a converged in-cylinder residual fraction, and to achieve a converged RANS ensemble velocity field. Responses were recorded for each cycle and included in the database, with the cycle number as the seventh parameter of a discrete nature. Seven predictors and 25 data points per predictor resulted in a dataset of 180 points. The CFD database thus formed served as the training set for building the GPR models.

There were two reasons behind the decision to use the data from the first and second simulation cycles: (1) use GPR models to understand the impact of cycle number on responses such as emissions, internal residual fractions, etc., and understand how many cycles are essential to achieve convergence on these responses. Results from this part of the research are not included in the current manuscript; (2) simulating three cycles of each sample point with the models and mesh set-up explained earlier took approximately 6 days with 2 nodes (16 cores per node, 8 GB per core). This was the primary limiting factor in deciding a relatively smaller size of the Latin hypercube dataset. It is because of the same reason, the results from the first two cycles were included in

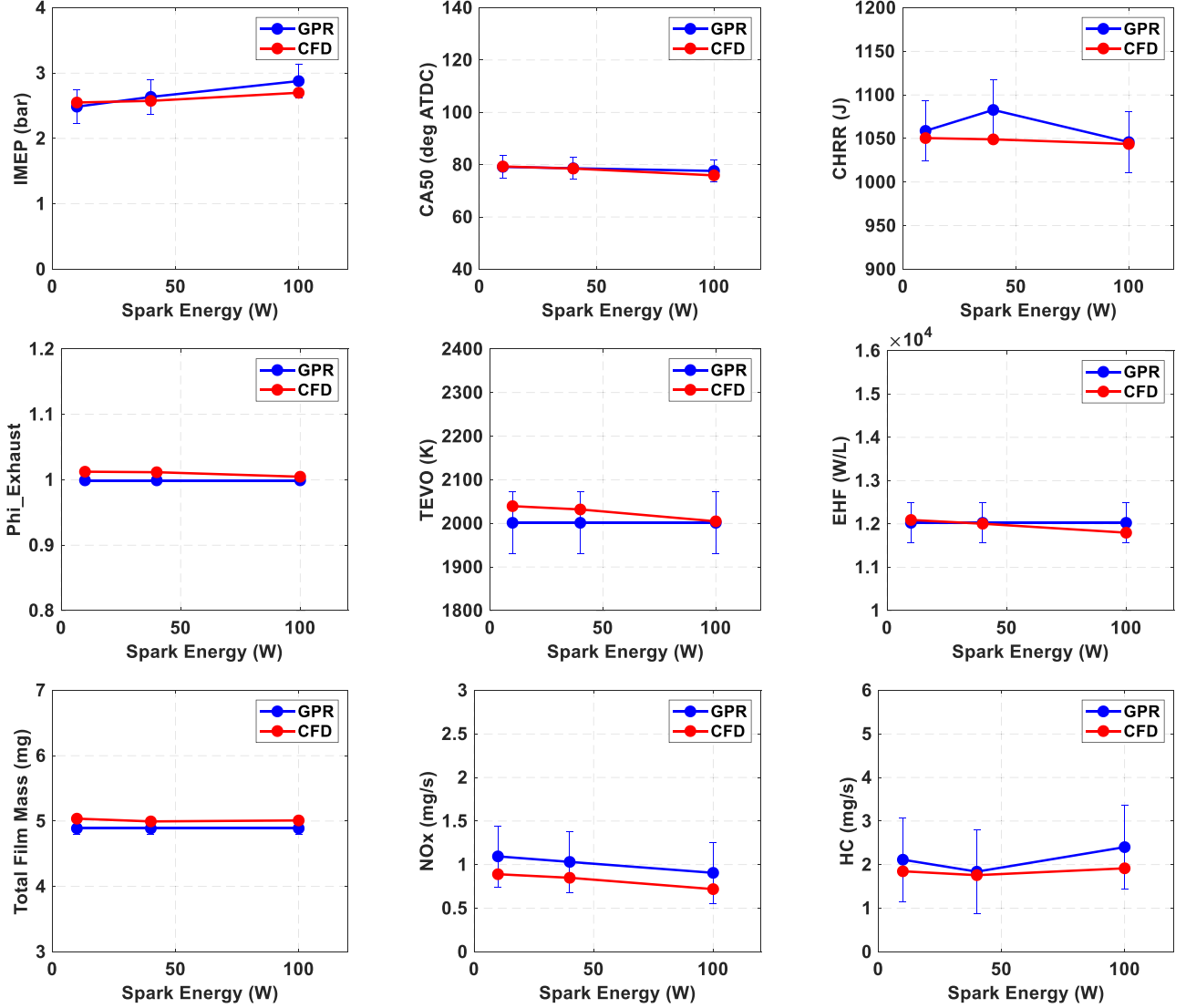


Fig. 6. GPR predictions for spark energy sweep validated against CFD results.

the dataset instead of discarding them as usually followed in the RANS simulations.

Results and discussion

GPR model training and uncertainty quantification

GPR model training was performed using MATLAB. As mentioned before, Test #2 was taken as the baseline case for this study. The non-parametric dataset framed using the CFD results served as the training set. The parameters presented in Table 9 along with the simulation cycle number were used as the set of seven predictors. Separate GPR models were trained for nine response functions of interest: NOx, HC, Phi_Exhaust, IMEP, CA50, EHF, total film mass, TEVO, and CHRR. The issues of overfitting were avoided by using the cross-validation technique, k-fold [40], using a value of 5. The first attempt was to train the GPR models using the kernel functions provided in Table 7, which assumed equal weights for all of the predictors. This practice failed to give acceptable R^2 (or root mean square error, RMSE) values for all response variables because the models failed to capture the varying sensitivity of one predictor over another. For example, NOx can have a higher sensitivity to spark timing than to injection pressure or spark energy. Similarly, wall films will have a higher sensitivity to injection pressure over

spark energy or intake manifold pressure. A solution to this problem was the use of the advanced kernel functions, shown in Table 8, with a separate length scale for each predictor. Where they were required, further improvements to the RMSE values were made possible by combining more than one kernel function. Table 11 lists the kernel function combination used for each response variable. The corresponding RMSE values will be later used to quantify the uncertainty associated with the GPR model of each response variable in the upcoming validation plots.

GPR model validation for response variables

In this section, the GPR model predictions will be compared with the CFD results, both generated for the same validation set. At this point, it is important to emphasize a principle difference between these two modeling methodologies. While it takes approximately six days to generate each three-cycle CFD result, the GPR results were generated in a matter of seconds. Table 12 shows the validation set of 15 cases, which includes the sweep of all the predictor parameters listed in Table 9. Test #2 from Table 3 was used as the baseline for performing this sweep. CFD simulations at each of these points were performed for three cycles. The validations presented here compare the GPR and CFD model responses from the third cycle.

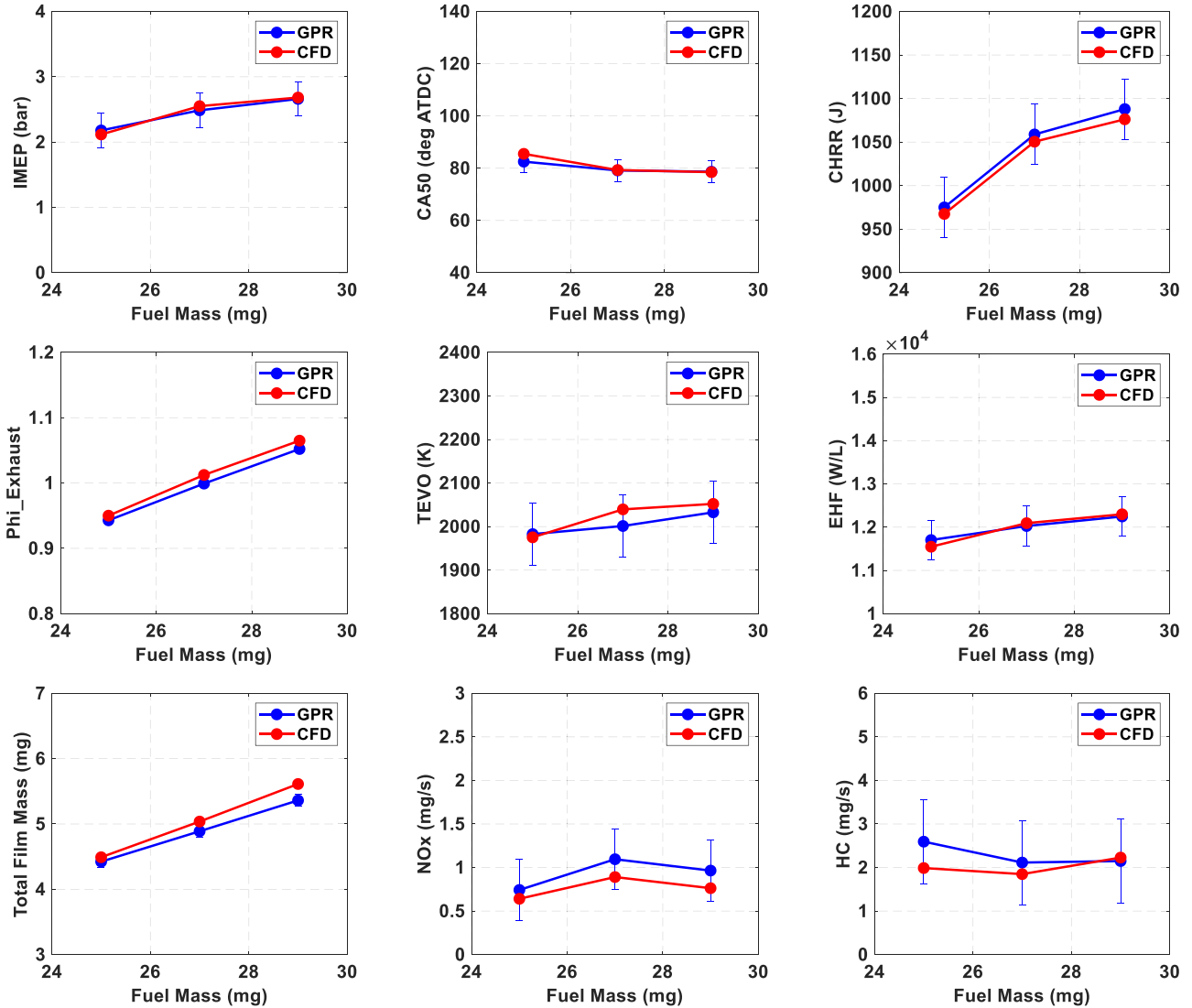


Fig. 7. GPR predictions for fuel mass sweep validated against CFD results.

Fig. 3 compares the GPR predictions to the CFD results for the EOI2 sweep. The GPR model did an excellent job of capturing the CFD trends for a changing EOI2. It was shown that EOI2 has a significant influence on all variables with a relatively lower influence on the Phi_Exhaust. An early EOI2 leads to an increased wall-film formation because of the increased wall area exposed to the incoming spray. The first and second spray injection details appear in Table 3. For EOI2 of 25 deg, around 25% of the total injected fuel was left behind as wall films. Although not shown here, 87.3% of these films were formed on the piston surface, 12.5% on the liner, and the remaining 0.2% on the head. The film mass values presented here were reported at the end of the cycle after considering the different aspects of wall-film interactions, such as splash, rebound, and evaporation. The increased wall film contributed significantly to the increase in HC emissions. The increased wall film reduced the fuel available for combustion, the effect of which could be seen from the reduced CHRR, retarded CA50, and reduced load. The more retarded CA50 resulted in an increased TEVO and an increased exhaust heat flux, which came at a mild penalty in NOx.

Fig. 4 compares the GPR predictions to the CFD results for the injection pressure (IP) sweep. The GPR model adequately captured the CFD trends, except for the over-prediction of the IMEP values at higher IPs. Higher injection pressure helped with reduced film formation, resulting in a reduced HC formation. Injection pressure did not have a significant

influence on NOx, EHF, Phi_Exhaust, or TEVO. A closer look showed that the load increasing with IP from 150 to 200 bar and then marginally decreasing as IP reached the high value of 400 bar. The reason for this could be understood from the CA50 and CHRR trends.

Fig. 5 compares the GPR predictions to the CFD results for the spark timing sweep. The GPR model predictions were in excellent agreement with the CFD trends. A retarded spark timing resulted in a delayed CA50 and an increased TEVO. Although it helps to achieve a higher EHF, the penalty of reduced combustion efficiency, as seen from the cumulative heat release plot, was a drop in the IMEP. NOx, directly correlated with temperature, increased because of the increase in TEVO and a decrease in the internal residual fraction due to the lower density of the exhaust gases. The increase in HC emissions with retarded spark timing is the result of the poor combustion, as evident from the dropping CHRR and IMEP, leading to an increased quantity of unburned fuel left at the EVO. A change in spark timing did not influence total film formation and Phi_Exhaust. Delayed spark timing is much preferred under the cold-start conditions for boosting the exhaust heat flux, which helps with the rapid light-off of the after-treatment system. However, the associated penalty of reduced load and increased NOx must be handled via carefully optimizing the rest of the operating parameters.

Fig. 6 compares the GPR predictions to the CFD results for the spark energy sweep. The GPR model does a good job of capturing the rela-

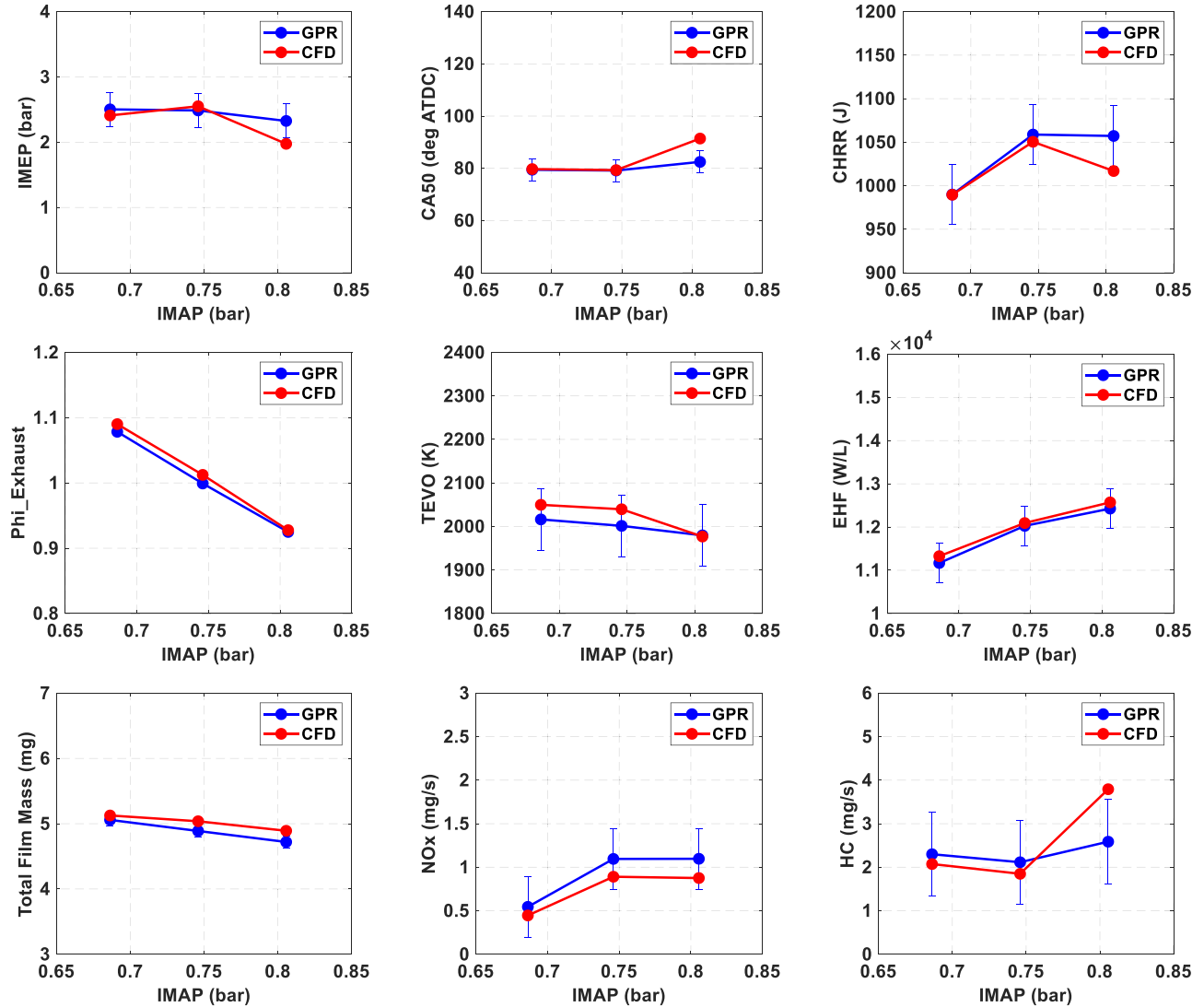


Fig. 8. GPR predictions for IMAP sweep validated against CFD results.

Table 13

Factors and levels considered for developing the full factorial DOE to be used as input for the trained GPR models.

EOI2 (deg BTDCc)	20	30	40	50	60	70	80				
Injection pressure (bar)	150	200	250	300	350	400	450				
Spark timing (deg ATDCc)	14	16	18	20	22	24	26	28	30	32	34
Spark energy (W)	10	50	100								
Fuel mass (mg)	24	25	26	27	28	29	30				
IMAP (bar)	0.68	0.7	0.72	0.74	0.76	0.78	0.8	0.82			

tively subtle effects produced by the changing spark energy. The expected spark energy did not seem to have a noticeable effect on film formation and Phi_Exhaust.

Fig. 7 compares the GPR predictions to the CFD results for the fuel mass sweep. The GPR model did an excellent job of predicting fuel mass trends. As seen from the figure, a higher fuel mass led to an increased film formation. However, HC emissions did not seem to follow the film trend, as observed with EOI2. This indicated that the trends produced by changing fueling must be observed closely. With an increase in fueling from 25 to 27 mg, a favorable stratified mixture was produced inside the cylinder. This was evident from the increasing cumulative heat release and the advancing CA50. The result was a lower unburned fuel mass at the EVO, which helped with controlling the HC emissions. The

increased cumulative heat release helped, with a higher TEVO resulting in an increased NOx. On the other hand, when the fueling increased from 27 to 29 mg, combustion efficiency dropped, as shown in the reducing cumulative heat release and the increasing slopes of the CA50 trends. Moreover, HC emissions increased because of poor combustion as the result of the richer mixture, leading to a larger quantity of unburned fuel mass at the EVO. In addition, the TEVO and NOx trends strictly followed the CA50 trends. Finally, the changing fuel mass had a major effect on the Phi_Exhaust as well.

Fig. 8 compares the GPR predictions to the CFD results for the intake manifold pressure (IMAP) sweep. The IMAP had a substantial effect on all of the responses. For instance, a 10% lower IMAP (than the baseline value of 74,594 Pa or ~0.75 bar) resulted in a rich mixture,

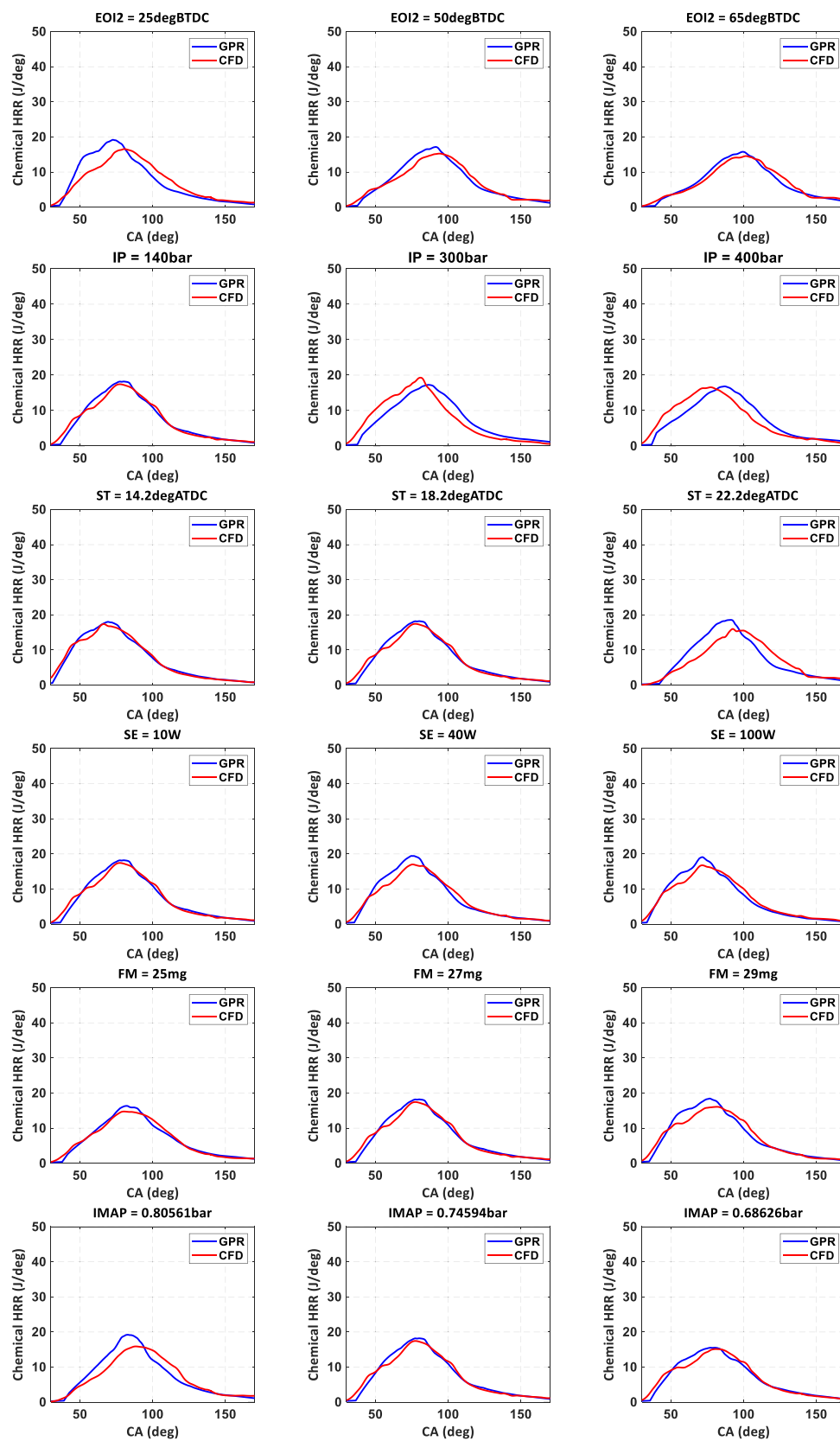


Fig. 9. GPR predictions of chemical heat release rates compared with CFD results.

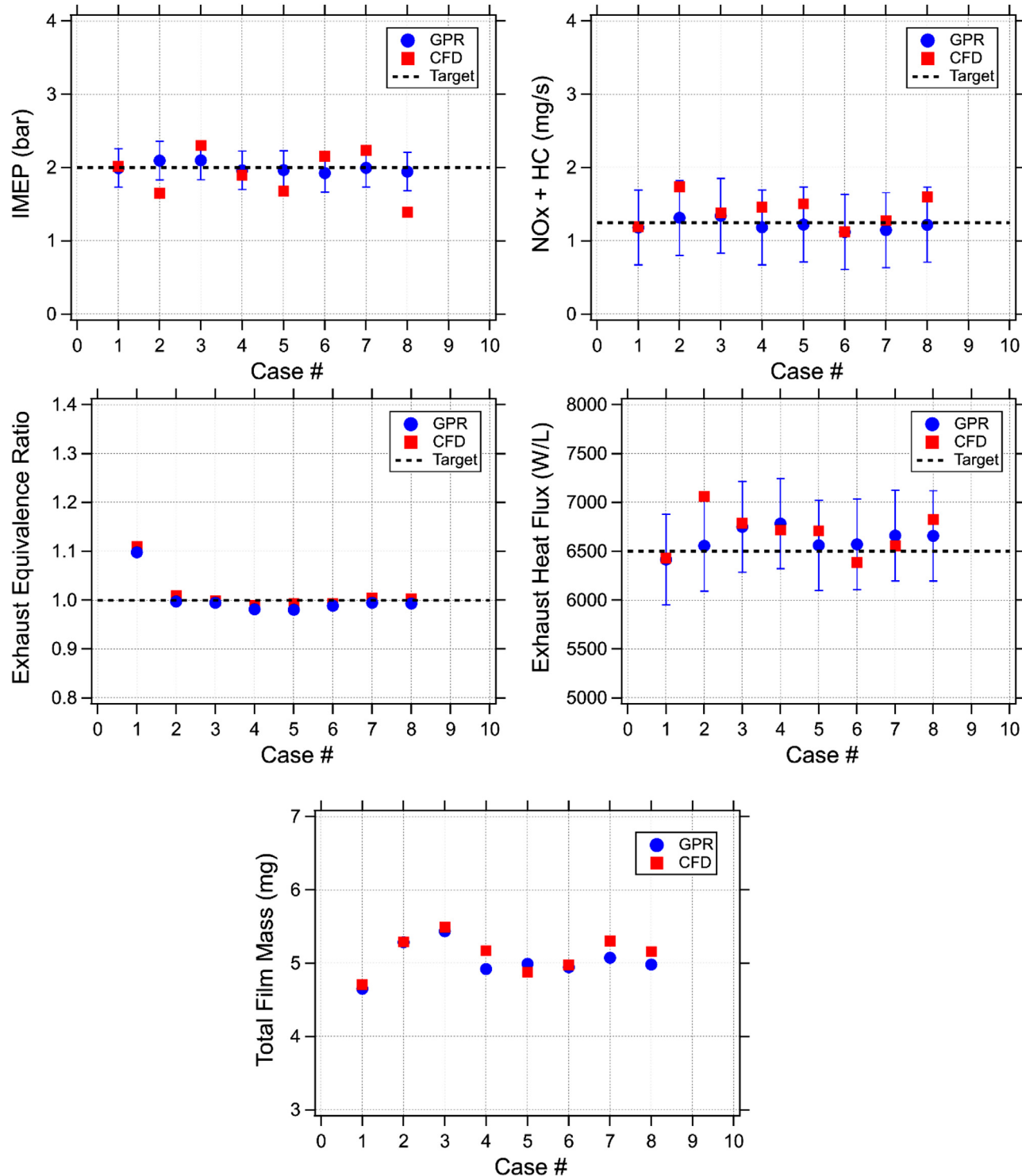


Fig. 10. GPR predictions for meeting the cold-start operating constraints validated against CFD results for the eight cases presented in Table 14.

leading to poor combustion, as evident from the dropping CHRR. This resulted in reduced NO_x and increased HC emissions due to the higher concentration of unburned fuel at the EVO. Conversely, a 10% higher IMAP (than the baseline value of 74,594 Pa or ~ 0.75 bar) resulted in a lean mixture that produced the same effects as explained earlier. Notably, an increased IMAP and an increased fuel mass produce the opposite effect in the Phi_Exhaust. An increased IMAP resulted in an increased mass flow rate out of the exhaust, leading to an increased EHF.

GPR model validation for chemical heat release

This section will explore the idea of predicting the chemical heat release rates using the GPR modeling methodology. Two sets of GPR models were essential for this exercise. The first set of GPR models was trained for CA1, CA2, and so forth, representing 1% and 2% of the chemical heat release, respectively, all the way up to CA100. All of the models used the same kernel function, Matern5/2. The R^2 /RSME values obtained for CA10, CA50, and CA90 were 0.93/3.78 deg, 0.91/5.01 deg,

Table 14

Operating conditions identified by the GPR model meeting the mandated constraints for the cold-start phase.

Case	EOI2 (deg BTDCc)	Injection Pressure (bar)	Spark Timing (deg ATDCc)	Fuel Mass (mg)	IMAP (bar)	NOx+HC (mg/s)	Phi Exhaust	IMEP (bar)	EHF (W/L)
1	20	450	24	28	0.70	1.18	1.10	1.99	6417
2	70	300	14	27	0.76	1.32	1.00	2.10	6557
3	80	350	14	28	0.78	1.34	0.99	2.10	6752
4	80	450	16	27	0.76	1.18	0.98	1.96	6783
5	70	400	16	26	0.74	1.22	0.98	1.96	6562
6	80	300	16	26	0.74	1.12	0.99	1.92	6572
7	80	300	14	27	0.76	1.15	0.99	1.99	6660
8	70	200	16	26	0.74	1.22	0.99	1.94	6657

0.89/5.38 deg, respectively. The second set included the GPR model trained for the cumulative value of the chemical heat release, which used Matern3/2 as the kernel function to get an R^2 /RSME value of 0.90/34.2 J. These two model sets could then be used for predicting the chemical heat release rates.

Fig. 9 shows the GPR predicted chemical heat release compared with the CFD results for the same validation set presented in Table 12. These comparisons were made for the responses from the third cycle. The critical characteristics defining a heat release—such as CA10 (0–10% burnt mass fraction), CA50 (50% burnt mass fraction), CA90 (90% burnt mass fraction), peak and duration of the chemical heat release—were adequately captured by the GPR model. The changes in slope during the compression phase resulting from the flame impinging on the liner and the expansion phase resulting from effects such as wall heat transfer were captured well on multiple occasions. The results were quite promising for the relatively smaller size of the dataset used for the study. However, the need for a larger dataset was evident from the mismatches observed for the injection pressure trends. The plots also suggest the need for training GPR models at a much finer resolution for crank angles less than CA10 to produce closer matches in the early part of the chemical heat release rates.

Using the GPR models for meeting cold-start constraints

The extensively validated GPR models were used to predict the parameter values, which could meet the multiple constraints mandated for the cold-start fast-idle condition provided in Table 1. The absolute values of the CFD-modeled NOx, HC, and EHF did not match with the test numbers, as shown in Fig. 13 and Fig. 14, provided in the appendix. Consequently, for the current exercise, the absolute values of the GPR predictions for these responses were matched with the test values using appropriate scaling factors.

At this point, the validation set of 45 cases (15 cases X 3 cycles) was combined with the previous training set of 180 cases (60 cases X 3 cycles) to form a new CFD database of 225 cases (75 cases X 3 cycles). The GPR models were retrained using the same kernel functions on the larger dataset to improve the predictions. This exercise helped improve the R^2 value for responses such as NOx and HC to 0.815 (from 0.80) and 0.82 (from 0.80), respectively. The input dataset of the GPR models was framed using a full factorial design of the experiment (DOE) of parameters listed in Table 9. Table 13 shows the levels considered for each parameter to form a design space of 107,016 data points. In addition, Table 14 shows the data points that were filtered from the design space for meeting the mandated constraints on IMEP, exhaust equivalence ratio, exhaust heat flux, and emissions (NOx and HC). The spark energy for all the cases was 100 W.

Validating the GPR predictions with CFD

In this section, the GPR predicted conditions were simulated again in the CFD, to confirm whether the cold-start constraints were met. Fig. 10 shows the CFD results from the 3rd cycle compared with the GPR predictions. The error bars represent the uncertainty associated

with the respective GPR model, as obtained from the larger dataset. The comparisons were promising, except for a few outliers. For instance, the GPR model seems to have over-predicted the IMEP for Cases 8 and 2. In addition, the EHF was under-predicted by the GPR model for Case 2; however, it was above the mandated constraint value. On the other hand, the remaining GPR predictions appear to be in excellent agreement with the CFD results. The film mass estimated at the end of the cycle, while meeting the essential constraints for the cold-start, was observed to be around of 20% of the total injected fuel. These outliers were attributed to the relatively smaller dataset considered for this study. The solution would be to keep adding to the database so that the GPR models have a larger training set for making the next set of predictions. The additional eight CFD cases generated for this validation increased the CFD database to 249 points (83 cases X 3 cycles). Fig. 11 shows the GPR-predicted chemical heat release compared with the CFD results for the third cycle. CA10, CA50, CA90, the peak, and the duration of the chemical heat release were adequately captured by the GPR model. The changing slope during the compression phase resulting from the flame impinging on the liner and the expansion phase resulting from effects such as wall heat transfer were well captured.

Summary and conclusions

The current study demonstrated the strategy of combining CFD modeling with advanced Gaussian process regression (GPR)-based machine learning models to make predictions about DISI cold-start behavior with acceptable accuracy and a substantially reduced computational time. Multiple challenges must be addressed for optimizing a DISI engine performance for the cold-start phase: (1) maintaining a stoichiometric equivalence ratio (based on carbon-to-oxygen atoms) at the exhaust for the efficient operating of the after-treatment system; (2) reducing the NOx and HC emissions; and (3) ensuring enough exhaust heat flux for a rapid light-off of the after-treatment system, all while maintaining a fixed load of 2 bar IMEP (BMEP of 0 bar). Performing such a convoluted optimization process via multi-cycle CFD simulations alone would have been an arduous task. The solution would be to employ machine learning algorithms to assist CFD to speed up the optimization process with a minimal penalty in accuracy. The following are the main conclusions from this study:

- 1 Predictions from the GPR models trained on a relatively smaller dataset compared well with the CFD results. The credit for the adequate predictions was attributed to the kernel functions used with the GPR models.
- 2 The trained GPR models successfully predicted the operating conditions that would meet the essential cold-start operating constraints on the IMEP, exhaust heat flux, and emissions (NOx and HC).
- 3 The GPR vs CFD model validations presented in this paper became more intriguing with the inclusion of the computational timescales comparison associated with these simulations. Each CFD result was generated in approximately six days, whereas it took a few seconds to produce the GPR model predictions.

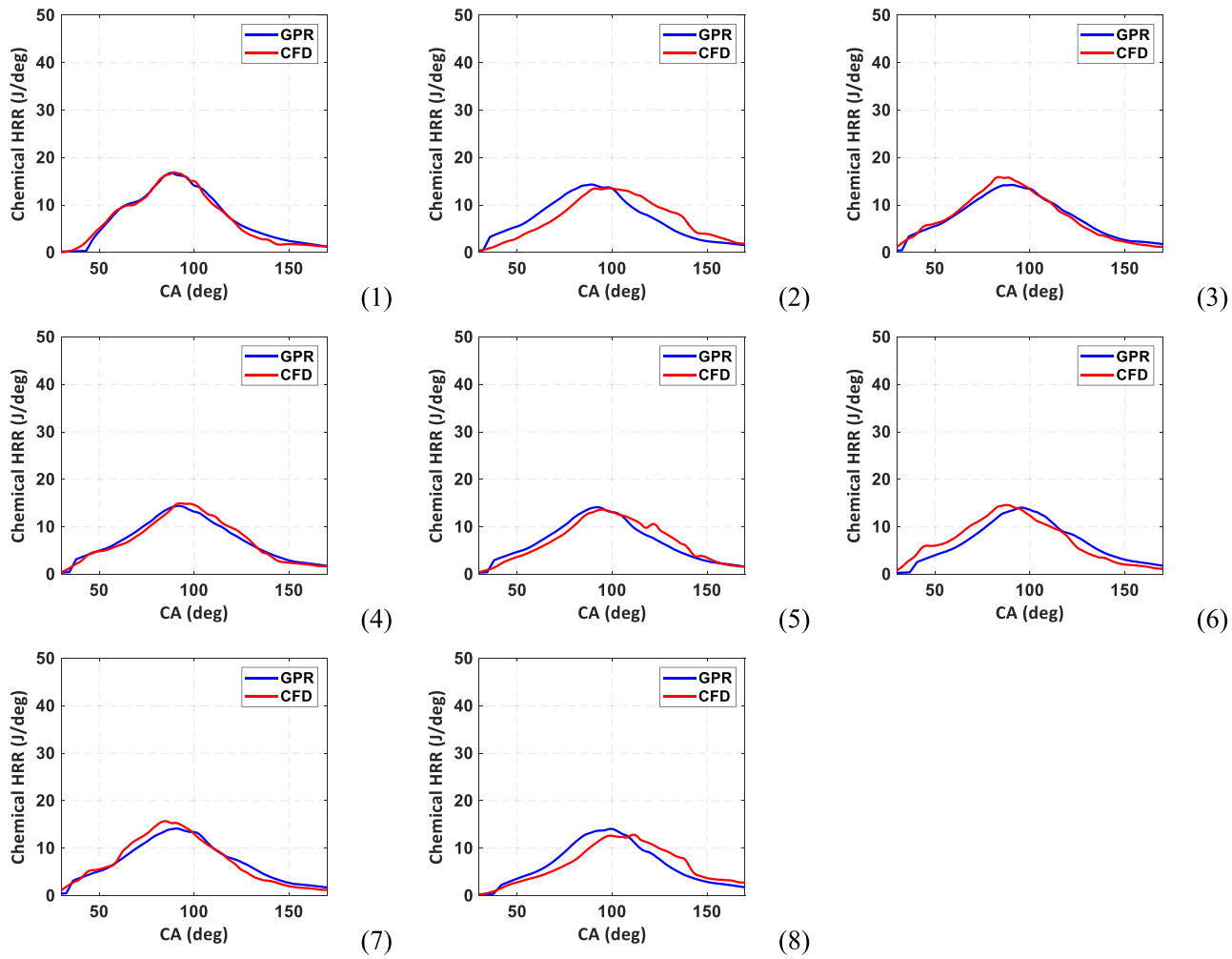


Fig. 11. CFD chemical heat release rates compared with GPR predictions for the eight cases presented in Table 14.

The idea of this work was to demonstrate an approach in which the machine learning algorithms could be effectively used to assist CFD simulations in tackling convoluted optimization problems with acceptable accuracy and a substantially reduced computational time. It should be understood that the GPR models demonstrated here are of stochastic nature, meaning the physics behind the interactions were not modeled. For example, the effect of increasing wall films on HC formation was well captured by the GPR model, but the physics behind such interactions has not been modeled. Hence, such ML models cannot replace the explicit CFD simulations, but they could be effectively used for expediting CFD-based problem-solving, as presented in this paper.

Declaration of Competing Interests

The authors declare that they have no known competing financial interests or personal relationships that could have appeared to influence the work reported in this paper.

Acknowledgments

This material was based upon work supported by Ford Motor Company's University Research Program (URP). The authors would like to thank Benjamin Petersen from Ford for his insightful input. In addition, the authors wish to thank Convergent Science Inc. for providing the licenses for the CONVERGE CFD solver. We are also grateful to the Center for High Throughput Computing (CHTC) at UW-Madison for providing

computing resources and to Joshua Leach for administering the computer systems in our Engine Research Center.

Appendix

CFD Model Validation

This section will compare the predictions of the CFD models to the experimental data for the three cold-start fast-idle conditions provided in Table 3. A total of three simulation cycles were run to remove the uncertainties associated with the initial conditions, obtain a converged value of the in-cylinder residual fraction and achieve converged ensemble-averaged velocity values from the RNG k- ϵ turbulence model. The results presented here are from the third cycle. An additional reason for stopping the simulations at the third cycle was the significant increase in the computational time resulting from the wall films, as explained in the introduction. Multiple-cycle experimental data for 300 cycles are shown, and Fig. 12 shows the pressure and apparent heat-release comparisons. The experiments were conducted at steady-state conditions (Table 3) that represented the catalyst-heating portion of the cold-start process. The oil and coolant supplied to the engine were controlled to 20 °C throughout the steady-state engine operation. The intake air was supplied to the engine at 20 °C. The GLR and PVG model predictions were in overall excellent agreement with the cold-start fast-idle experimental measurements for both of the engines. Beyond this, CA10 (a 0–10% burnt fuel mass fraction) of the spark advance and the phase of main combustion (CA50) were well predicted. The credit for the excellent predictions provided by the GLR model is also attributed to

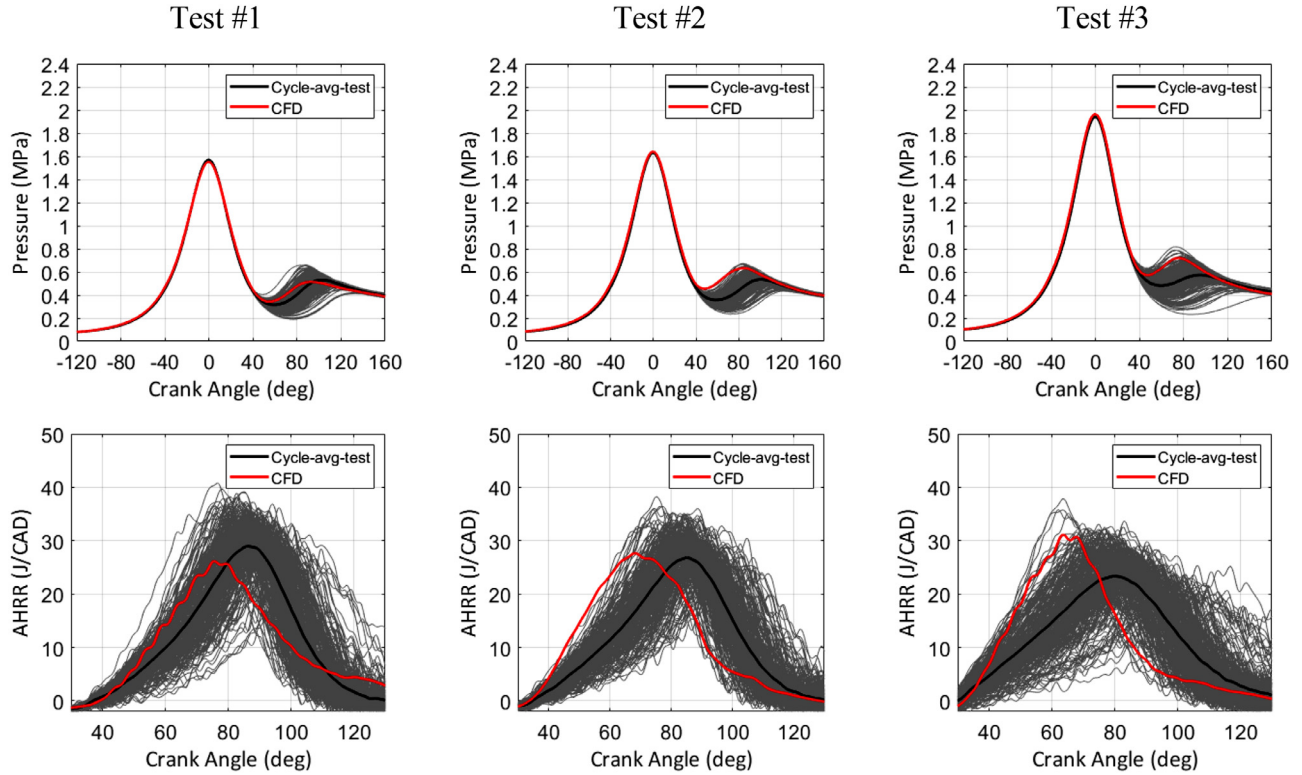


Fig. 12. CFD predictions compared to experimental pressure and apparent heat-release traces for three cold-start conditions of the SG-DISI 2.3 L engine. Details of Tests 1, 2, and 3 are provided in Table 3.

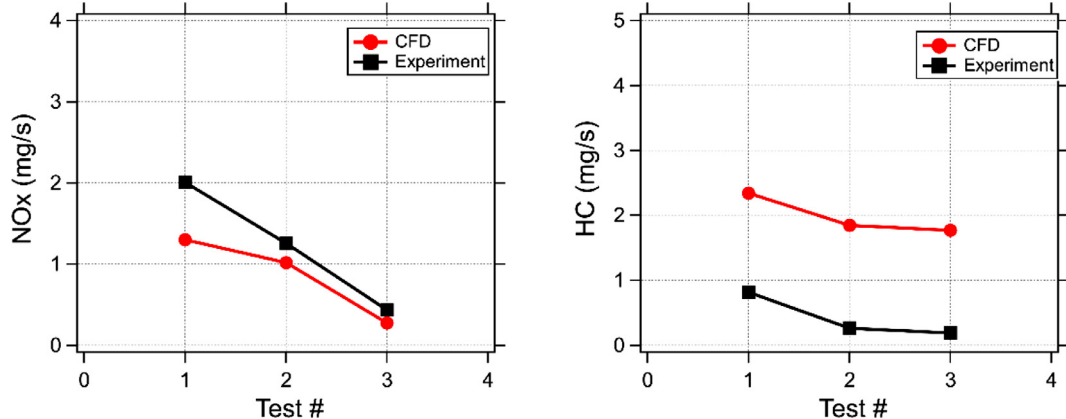


Fig. 13. CFD predicted NOx and HC emissions compared with measured data. Tests 1, 2, and 3 had EVO timings of 155 deg ATDCc, 180 deg ATDCc, and 205 deg ATDCc, respectively.

the robust models, which were responsible for capturing the wide array of phenomena occurring within the cylinder, leading to the process of combustion.

Fig. 13 compares the CFD emission predictions to the measured data. Both the Zeldovich NOx and HC emissions trends were in good agreement with the measured data. The mismatch in the absolute values resulted from the differences in the locations where these measures were reported. That is, the emission values from simulations were reported at the exhaust runner outlet, whereas the measurements were reported far downstream. Reduction in NOx with delayed EVO occurred because of the increased internal residual fraction resulting from the extended valve overlap. Tests 1, 2, and 3 showed EVO timings of 155 deg, 205 deg, and 180 deg ATDCc, as well as valve overlaps of 5 deg, 30 deg, and 55 deg, respectively. Accordingly, the internal residual fraction was calculated to respectively be approximately 4%, 10%, and 14%, ex-

plaining the NOx trends observed here. In addition, the HC emission trends could be understood from the explanations provided in the Section titled ‘Emissions modeling’. The HC reduction observed with delayed EVO was attributed to two reasons: (1) A delayed EVO ensured a longer residence time for the HC oxidation, and (2) This delayed EVO combined with a longer valve overlap (eg: 30 deg for Test #2) helped in re-breathing the outgoing unburned HC back into the cylinder and oxidizing it.

Fig. 14 shows the exhaust heat flux (EHF) predictions compared with the measured data. Although the EHF trend was adequately captured, the models seemed to be over-predicting the absolute values. This was because of two reasons: (1) the difference in the locations where the predicted and measured values were compared and (2) the effect of neglecting wall heat transfer from the point of exhaust valve opening to the point of heat flux measurements. The validations presented here

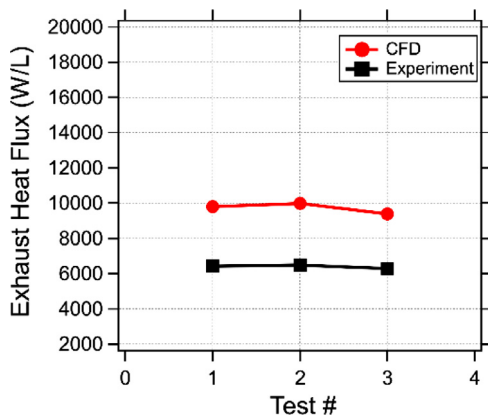


Fig. 14. CFD-predicted exhaust heat flux (EHF) compared with measured data.

confirm the effectiveness of the CFD models for optimizing the cold-start operating conditions.

References

- [1] Façanha C, Blumberg K, Miller J. Global transportation energy and climate roadmap: the impact of transportation policies and their potential to reduce oil consumption and greenhouse gas emissions. Washington, DC: The International Council on Clean Transportation; 2012.
- [2] LaHood R, Jackson LP. Final rule making for 2017-2025 light-duty vehicle greenhouse gas emission standards and corporate average fuel economy standards. EPA NHTSA; 2012. p. 3–24.
- [3] Davis S.C., Williams S.E., Boundy R.G., Moore S., 2015 vehicle technologies market report. Tech. rep. Oak Ridge, TN (United States): Oak Ridge National Lab.(ORNL), 2016.
- [4] Rodriguez JF, Cheng WK. Analysis of NO_x emissions during crank-start and cold fast-idle in a GDI engine. *SAE Int J Engines* 2017;10:646–55 <https://doi.org.ezproxy.library.wisc.edu/10.4271/2017-01-0796>.
- [5] Rodriguez JF, Cheng WK. Cycle-by-cycle analysis of cold crank-start in a GDI engine. *SAE Int J Engines* 2016;9:1210–19 <https://doi.org.ezproxy.library.wisc.edu/10.4271/2016-01-0824>.
- [6] Xu Z, Yi J, Wooldridge S, Reiche D, Curtis E, Papaoianou G. Modeling the cold start of the Ford 3.5L V6 ecoboost engine. *SAE Int J Engines* 2009;2:1367–87 <https://doi.org.ezproxy.library.wisc.edu/10.4271/2009-01-1493>.
- [7] Heywood JB. Internal combustion engine fundamentals. McGraw-Hill Education; 2018.
- [8] Aghdam EA, Burluka AA, Hattrell T, Liu K, Sheppard CGW, Neumeister J, Crundwell N. Study of cyclic variation in an SI engine using quasi-dimensional combustion model. SAE International; 2007. Technical Report <https://doi.org.ezproxy.library.wisc.edu/10.4271/2007-01-0939>.
- [9] Etheridge J, Mosbach S, Kraft M, Wu H, Collings N. A detailed chemistry multi-cycle simulation of a gasoline fueled HCCI engine operated with NVO. *SAE Int J Fuels Lubr* 2009;2:13–27 <https://doi.org.ezproxy.library.wisc.edu/10.4271/2009-01-0130>.
- [10] Kodavasal J, Abdul Moiz A, Ameen M, Som S. Using machine learning to analyze factors determining cycle-to-cycle variation in a spark-ignited gasoline engine. *J Energy Resour Technol* 2018;140 <https://doi.org/10.1115/1.4040062>.
- [11] Moiz AA, Pal P, Probst D, Pei Y, Zhang Y, Som S, Kodavasal J. A machine learning-genetic algorithm (ML-GA) approach for rapid optimization using high-performance computing. *SAE Int J Commer Veh* 2018;11:291–306 <https://doi.org/10.4271/2018-01-0190>.
- [12] Kavuri C, Kokjohn SL. Exploring the potential of machine learning in reducing the computational time/expense and improving the reliability of engine optimization studies. *Int J Engine Res* 2020;21:1251–70 <https://doi.org/10.1177/1468087418808949>.
- [13] Badra J, Sim J, Pei Y, Viollet Y, Pal P, Futterer C, Brenner M, Som S, Farooq A, Chang J. Combustion system optimization of a light-duty GCI engine using CFD and machine learning. *SAE Tech Pap* 2020 0148-7191. <https://doi.org/10.4271/2020-01-1313>.
- [14] Badra J, Khaled F, Tang M, Pei Y, Kodavasal J, Pal P, Owoyele O, Futterer C, Brenner M, Farooq A. Engine combustion system optimization using CFD and machine learning: a methodological approach. *internal combustion engine division fall technical conference*. American Society of Mechanical Engineers; 2019. <https://doi.org/10.1115/ICEF2019-7238>.
- [15] Owoyele O, Pal P. A novel active optimization approach for rapid and efficient design space exploration using ensemble machine learning. *J Energy Resour Technol* 2021;143 032307. <https://doi.org/10.1115/1.4049178>.
- [16] Bertram AM, Kong S-C. Computational optimization of a diesel engine calibration using a novel SVM-PSO method. *SAE Tech Pap* 2019 0148-7191 <https://doi.org/10.4271/2019-01-0542>.
- [17] Owoyele O, Pal P. A novel machine learning-based optimization algorithm (ActivO) for accelerating simulation-driven engine design. *Appl Energy* 2021;285:116455 <https://doi.org/10.1016/j.apenergy.2021.116455>.
- [18] Probst DM, Raju M, Senecal PK, Kodavasal J, Pal P, Som S, Moiz AA, Pei Y. Evaluating optimization strategies for engine simulations using machine learning emulators. *J Eng Gas Turbine Power* 2019;141. doi:[10.1115/1.4043964](https://doi.org/10.1115/1.4043964).
- [19] Zhang Q, Ogren RM, Kong S-C. Application of improved artificial bee colony algorithm to the parameter optimization of a diesel engine with pilot fuel injections. *J Eng Gas Turbine Power* 2017;139. doi:[10.1115/1.4036766](https://doi.org/10.1115/1.4036766).
- [20] S B, Y W. Application of gaussian process regression to prediction of thermal comfort index. ICEMI; 2013. p. 958–61.
- [21] Hultquist C, Chen G, Zhao K. A comparison of gaussian process regression, random forests and support vector regression for burn severity assessment in diseased forests. *Remote Sens Lett* 2014;5:723–32. doi:[10.1080/2150704X.2014.963733](https://doi.org/10.1080/2150704X.2014.963733).
- [22] Pasolli L, Melgani F, Blanzieri E. Gaussian process regression for estimating chlorophyll concentration in subsurface waters from remote sensing data. *IEEE Geosci Remote Sens Lett* 2010;7:464–8. doi:[10.1109/LGRS.2009.2039191](https://doi.org/10.1109/LGRS.2009.2039191).
- [23] Platt JC, Burges CJC, Swenson S, Weare C, Zheng A. Learning a gaussian process prior for automatically generating music playlists. *Advances in neural information processing systems*; 2002.
- [24] Clifton L, Clifton DA, Pimentel MAF, Watkinson PJ, Tarassenko L. Gaussian process regression in vital-sign early warning systems. 2012 annual international conference of the IEEE engineering in medicine and biology society; 2012. doi:[10.1109/EMBC20126347400](https://doi.org/10.1109/EMBC20126347400).
- [25] Dürichen R, Pimentel MAF, Clifton L, Schweikard A, Clifton DA. Multi-task gaussian process models for biomedical applications. IEEE-EMBS international conference on biomedical and health informatics (BHI); 2014. doi:[10.1109/BHI20146864410](https://doi.org/10.1109/BHI20146864410).
- [26] Richards KJ, Senecal PK, Pomraning E. Converge (version 2.3). Madison, WI: Convergent Science; 2015.
- [27] Malaguti S, Cantore G, Fontanesi S, Lupi R, Rosetti A. CFD investigation of wall wetting in a GDI engine under low temperature cranking operations. Tech rep SAE International; 2009. doi:[10.4271/2009-01-0704](https://doi.org/10.4271/2009-01-0704).
- [28] Malaguti S, Fontanesi S, Severi E. Numerical analysis of GDI engine cold-start at low ambient temperatures. Tech rep SAE International; 2010. doi:[10.4271/2010-01-2123](https://doi.org/10.4271/2010-01-2123).
- [29] Han Z, Reitz RD. Turbulence modeling of internal combustion engines using rmg κ - ϵ models. *Combust Sci Technol* 1995;106:267–95. doi:[10.1080/00102209508907782](https://doi.org/10.1080/00102209508907782).
- [30] Ravindran AC, Kokjohn SL, Petersen B. Improving computational fluid dynamics modeling of direct injection spark ignition cold-start. *Int J Engine Res* 2020 1468087420963982. <https://doi.org/https://doi.org/10.1177/1468087420963982>.
- [31] Gilder ÖL. Correlations of laminar combustion data for alternative si engine fuels. Tech rep SAE International; 1984. doi:[10.4271/841000](https://doi.org/10.4271/841000).
- [32] Amsden A. LANL: a block-structured kiva program for engines with vertical or canted valves. Los Alamos National Laboratory; 1999. Technical Report.
- [33] Ravindran AC. Numerical modeling of gasoline direct injection spark ignition engines during cold-start Phd thesis. University of Wisconsin-Madison; 2021.
- [34] www.sandia.gov/ecn, 2020, Engine Combustion Network.
- [35] Anand K, Ra Y, Reitz RD, Bunting B. Surrogate model development for fuels for advanced combustion engines. *Energy Fuels* 2011;25:1474–84. doi:[10.1021/ef101719a](https://doi.org/10.1021/ef101719a).
- [36] Peters N. The turbulent burning velocity for large-scale and small-scale turbulence. *J Fluid Mech* 1999;384:107–32. doi:[10.1017/S0022112098004212](https://doi.org/10.1017/S0022112098004212).
- [37] Peters N. *Turbulent combustion*. Cambridge university press; 2000.
- [38] Bradley D, Lau AKC, Lawes M, Smith FT. Flame stretch rate as a determinant of turbulent burning velocity. *Philos Trans Royal Soc Lond Ser A: Phys Eng Sci* 1992;338:359–87 <https://doi.org/10.1098/rsta.1992.0012>.
- [39] Fan L, Reitz RD. Development of an ignition and combustion model for spark-ignition engines. *SAE Trans* 2000;1977–89 <https://doi.org.ezproxy.library.wisc.edu/10.4271/2000-01-2809>.
- [40] Anguita D, Ghelardoni L, Ghio A, Oneto L, Ridella S. The 'k'in k-fold cross validation editors. ESANN; 2012.